Chapter 4: Observations: Changes in Snow, Ice and Frozen Ground

Coordinating Lead Authors: Peter Lemke, Jiawen Ren

Lead Authors: Richard Alley, Ian Allison, Jorge Carrasco, Gregory Flato, Yoshiyuki Fujii, Georg Kaser, Philip Mote, Robert Thomas, Tingjun Zhang

Contributing Authors: J. Box, D. Bromwich, R. Brown, G. Cogley, J. Comiso, M. Dyurgerov, B. Fitzharris, O. W. Frauenfeld, H. Fricker, H. Gudmundsson, C. Haas, J. O. Hagen, C. Harris, L. Hinzman, R. Hock, M. Hoelzle, P. Huybrechts, K. Isaksen, P. Jansson, A. Jenkins, I. Joughin, C. Kottmeier, R. Kwok, S. Laxon, D. MacAyeal, K. C. McDonald, H. Melling, A. Ohmura, A. Payne, T. Prowse, B. Raup, C. Raymond, E. Rignot, I. Rigor, D. Robinson, D. Rothrock, L. Shiyin, S. Smith, O. Solomina, D. Vaughan, J. Walsh, A. Worby, T. Yamada, L. Zhao

Review Editors: Roger Barry, Toshio Koike

Date of Draft: 12 August 2005

Notes: This is the TSU compiled version

Figures

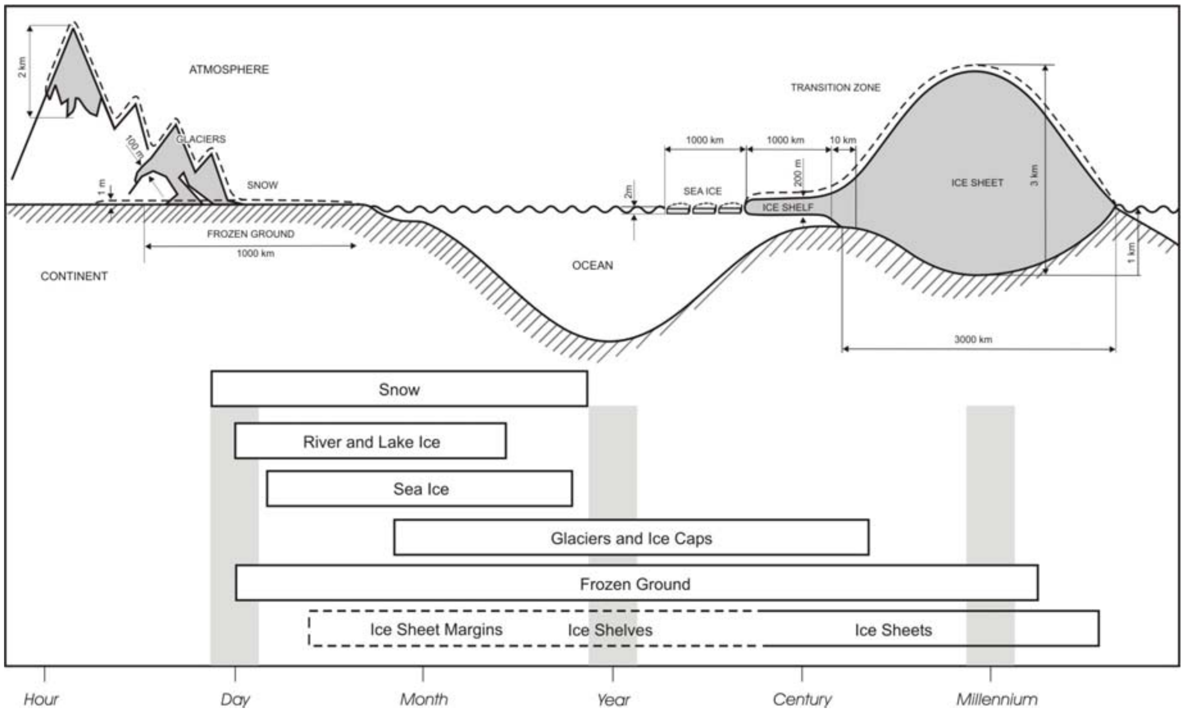

Figure 4.1.1. Components of the cryosphere and their time-scales.

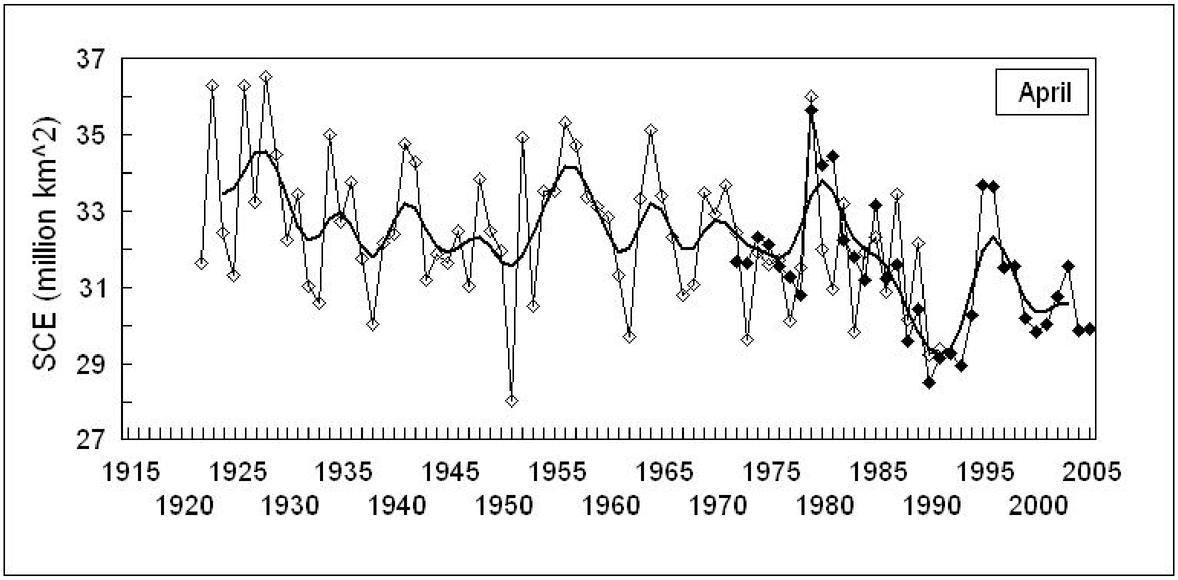

Figure 4.2.1. Update of NH April snow cover extent (SCE) from Brown (2000). Open diamonds are from the station-derived snow cover index of Brown (2000); solid diamonds are SCE values from the NOAA satellite dataset.

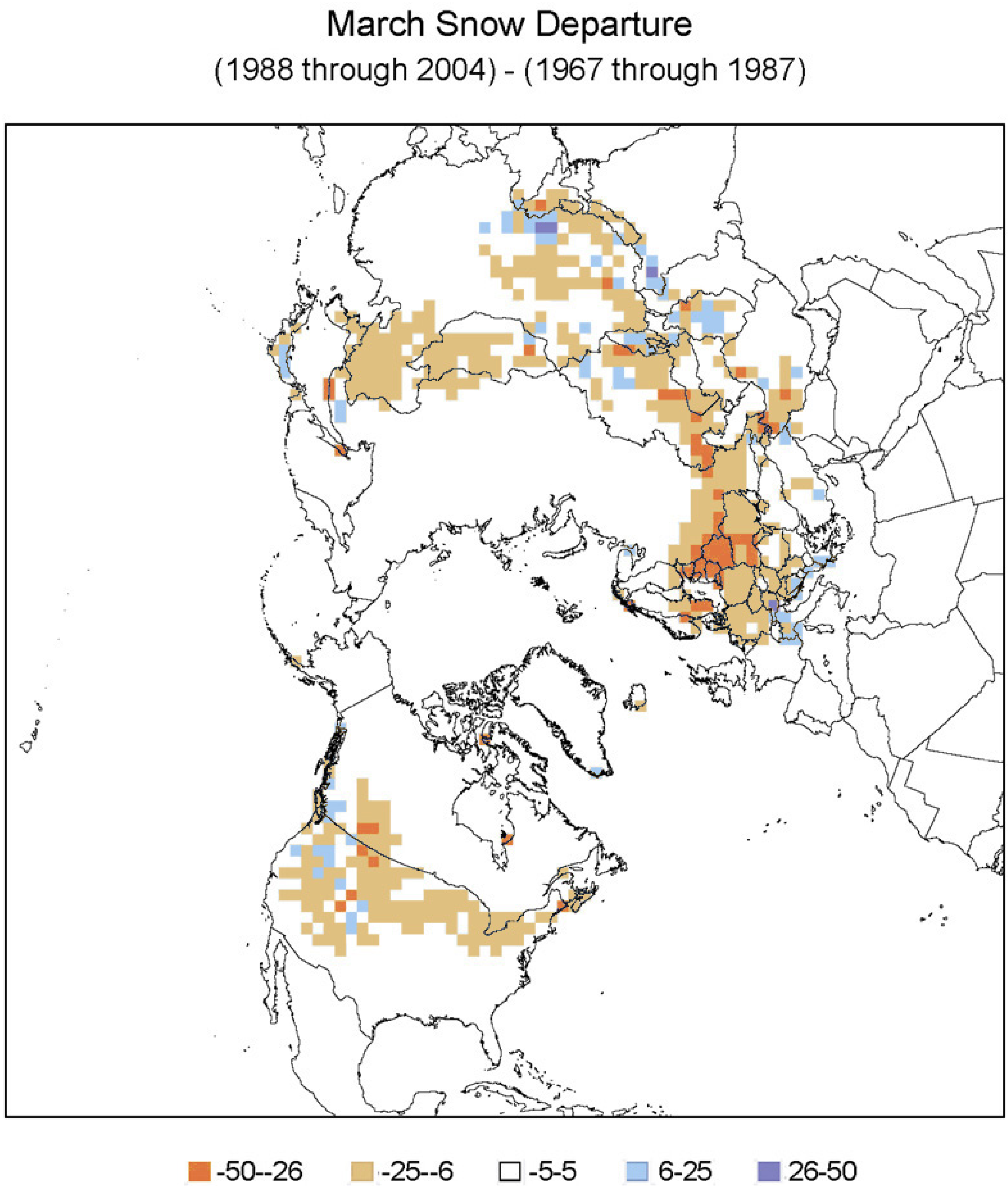

Figure 4.2.2. Differences in the distribution of March snow cover between earlier (1967–1987) and later (1988–2004) portions of the satellite era (expressed in percent coverage). Positive values indicate greater extent in the earlier portion of the record. Extents are derived from NOAA/NESDIS snow maps.

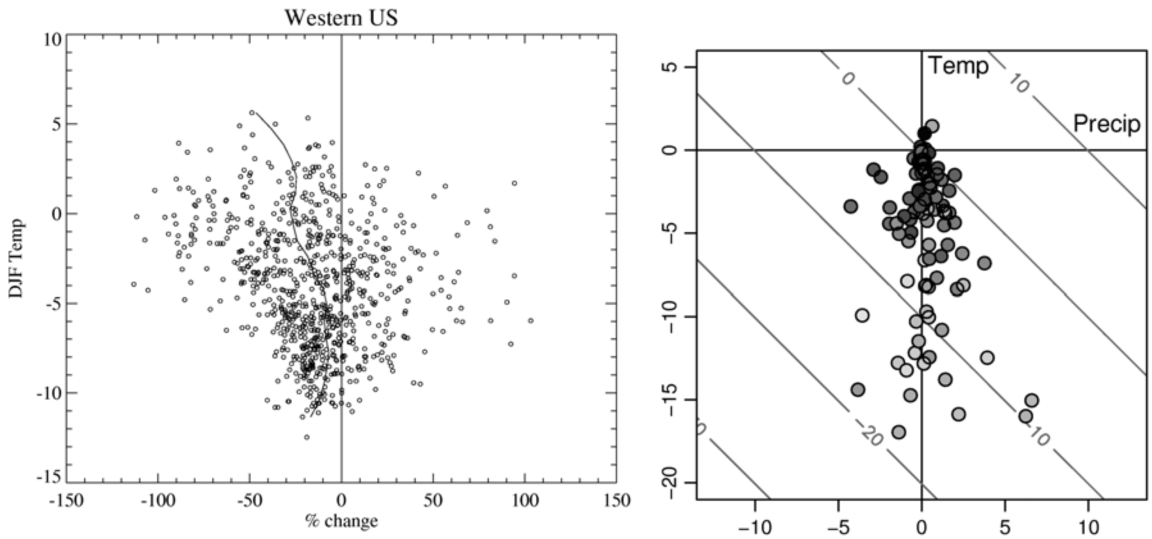

Figure 4.2.3. Dependence of trends in snow on elevation. (a) Relative trends in 1 April snow water equivalent, 1950–2000, in the mountains of the western US (west of the continental divide), binned by mean December–February temperature. Adapted from Mote et al. (2005). (b) Attribution of trends in snow cover days in Switzerland, 1958–1999, to precipitation (x-direction) and temperature (y-direction). Station altitude indicated by grayscale: darker is higher. From Scherrer et al., 2004.

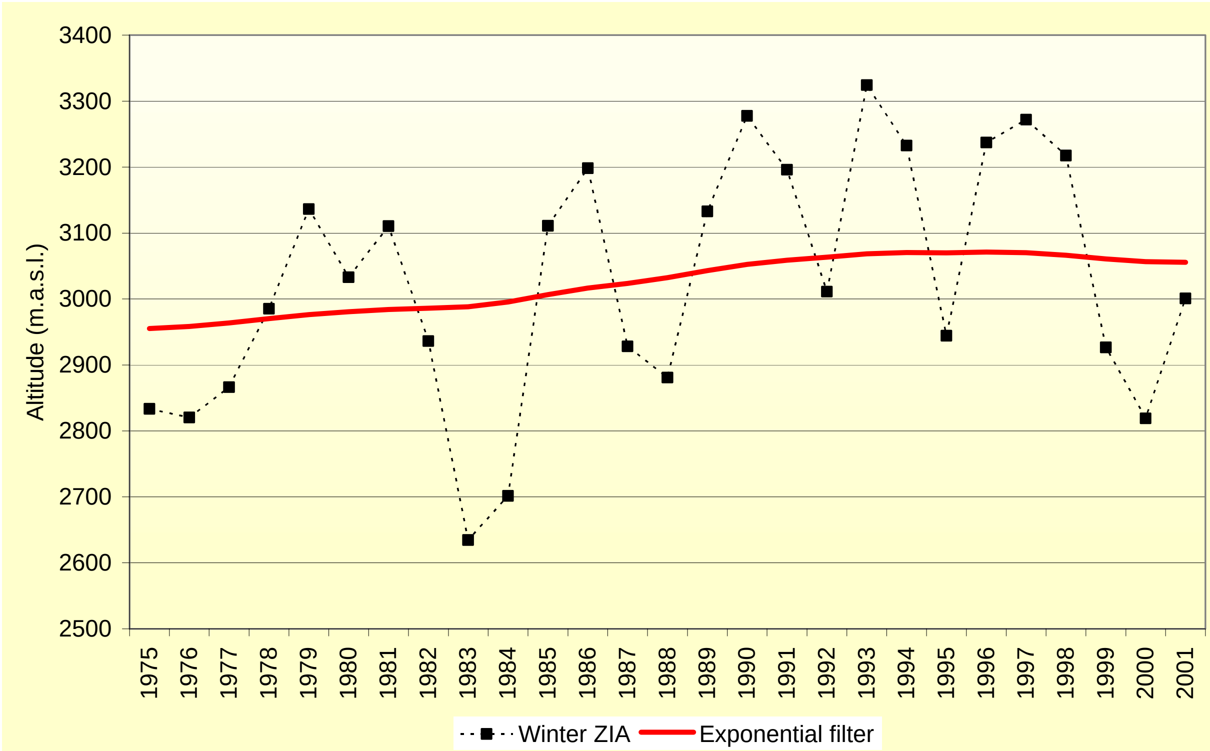

Figure 4.2.4. Altitude of winter 0°C isotherm (ZIA) in central Chile as derived directly from the radiosonde data at Quintero station (Carrasco et al., 2005), and (red) smoothed using an exponential filter.

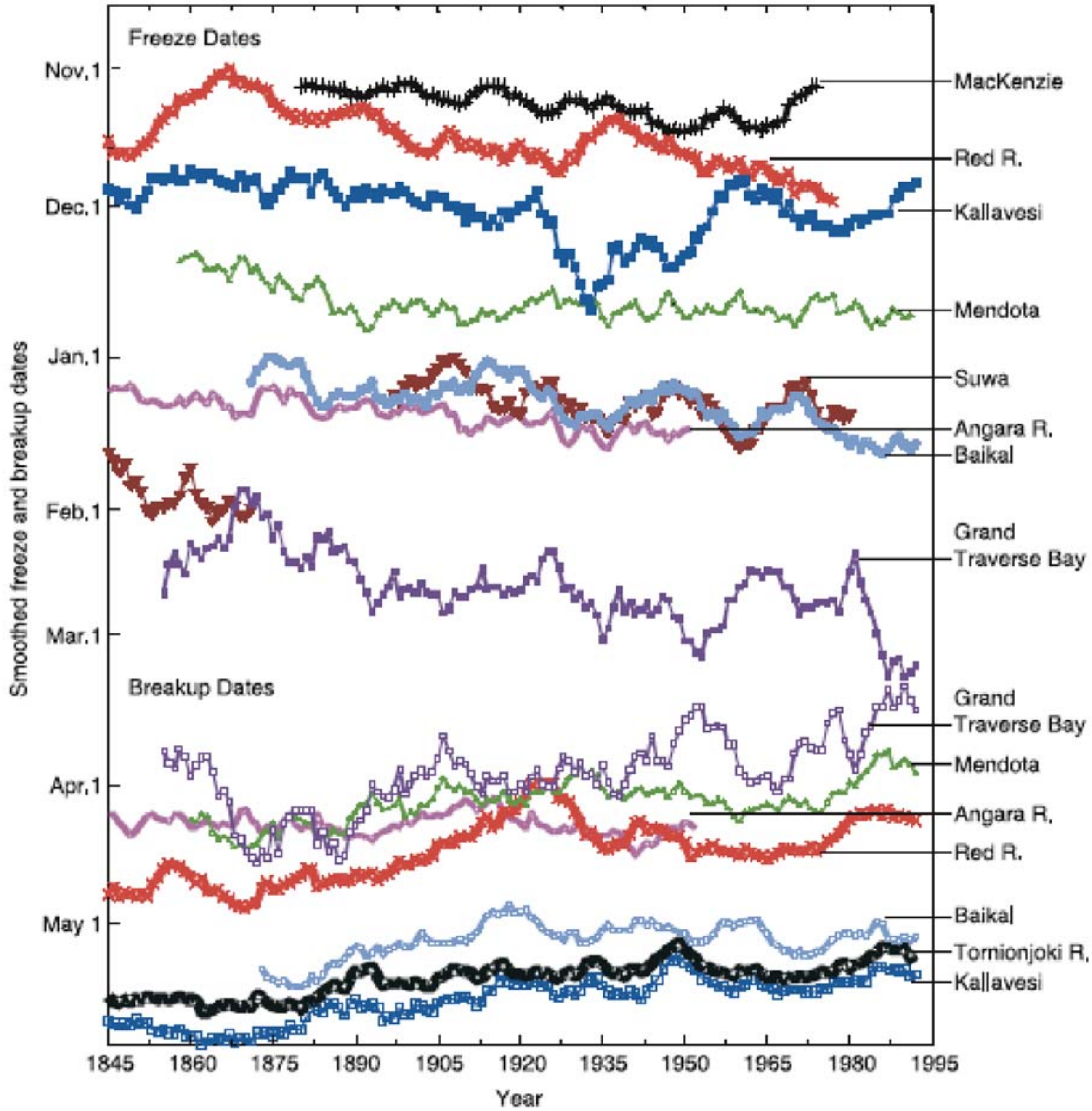

Figure 4.3.1. Time series of freeze-up and break-up dates from several northern lakes and rivers (from Magnuson et al., 2000). Dates have been smoothed with a 10-year moving average. See the cited publication for locations and other details.

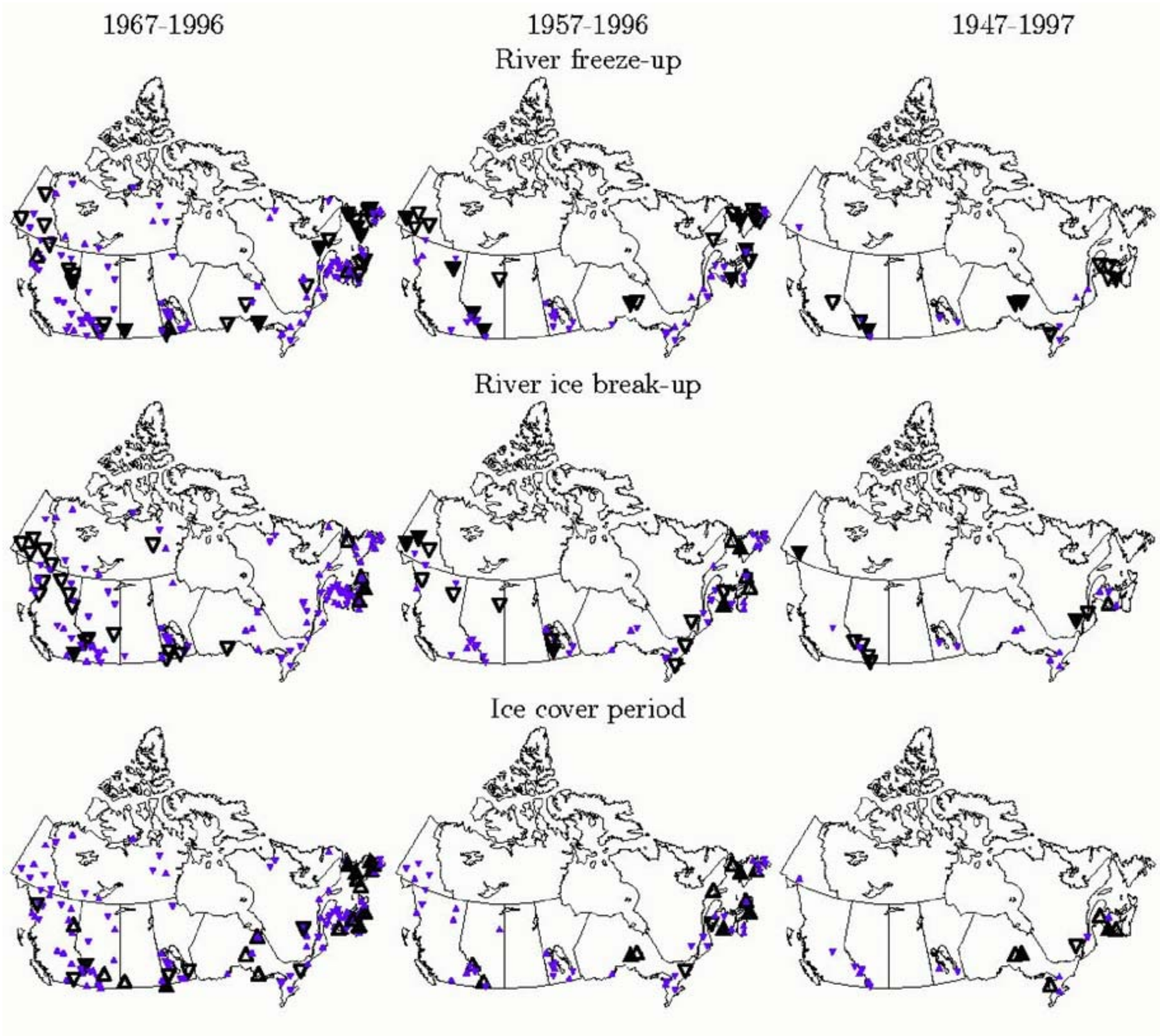

Figure 4.3.2. Trends in the dates of river freeze-up, river ice break-up, and periods of ice-cover. Upward pointing triangle indicates a delay to the beginning of the freeze-up or break-up periods; or to the lengthening of the ice-cover period. Downward triangle indicates an earlier occurrence to the start of the freeze-up or break-up periods; or to the shortening of the ice-cover period. Trends significant at the 1% and 10% levels are marked by larger filled and hollow triangles, respectively. Smaller triangles indicate that trends are not significant at the 10% level (Zhang et al., 2001).

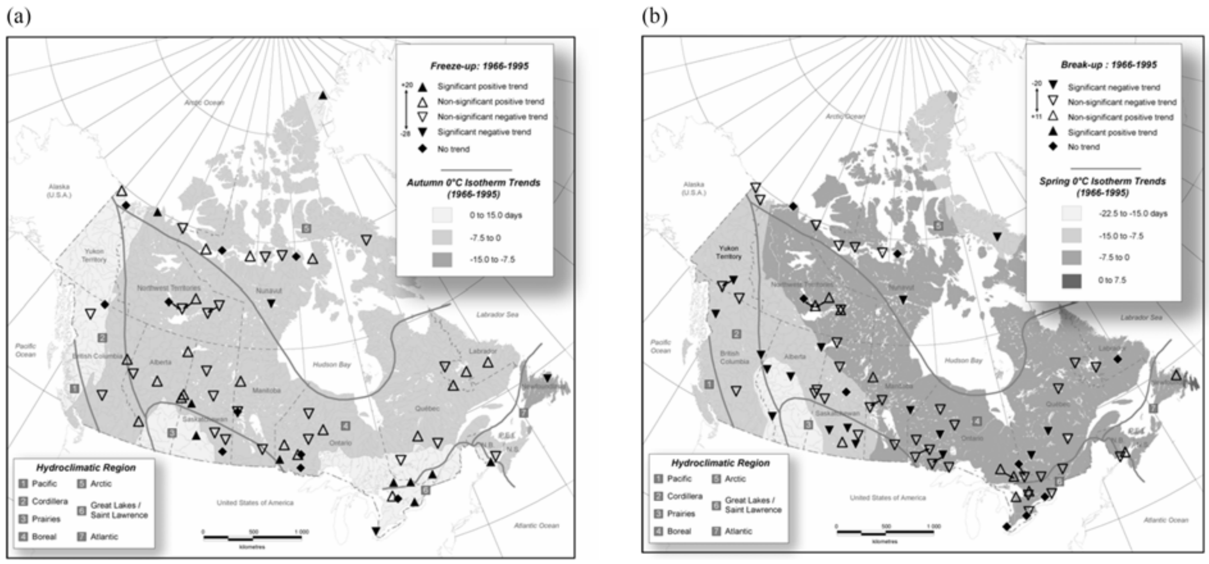

Figure 4.3.3. Trends in freeze-up and breakup dates observed at lakes in Canada over the period 1965–1995. Downward pointing arrows indicate a negative trend; upward pointing arrows a positive trend. Open symbols indicate that the trend is not significant while solid symbols indicate that the trend is significant at the 10% level. The shading indicates the trend in date when the zero-degree temperature threshold is crossed. From Duguay et al. (submitted).

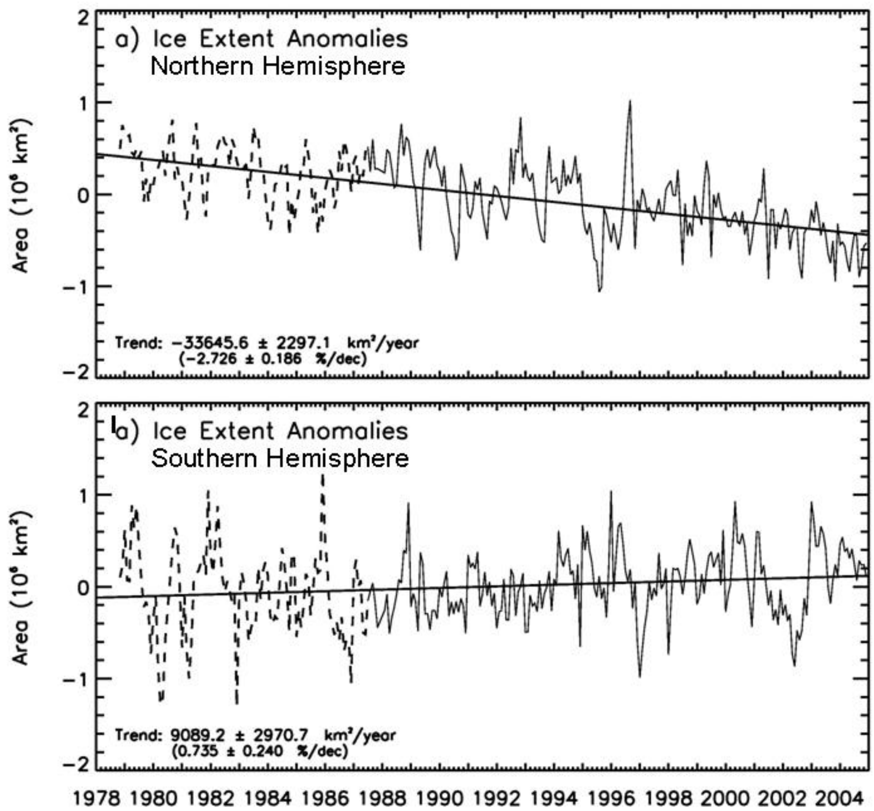

Figure 4.4.1. Sea Ice extent anomalies for (a) Northern Hemisphere and (b) the Southern Hemisphere based on passive microwave satellite data. Linear trend lines are indicated for each hemisphere. The negative trend in the Northern Hemisphere is significant at the 95% confidence level whereas the small positive trend in the Southern Hemisphere is not significant. (Updated from Comiso, 2003).

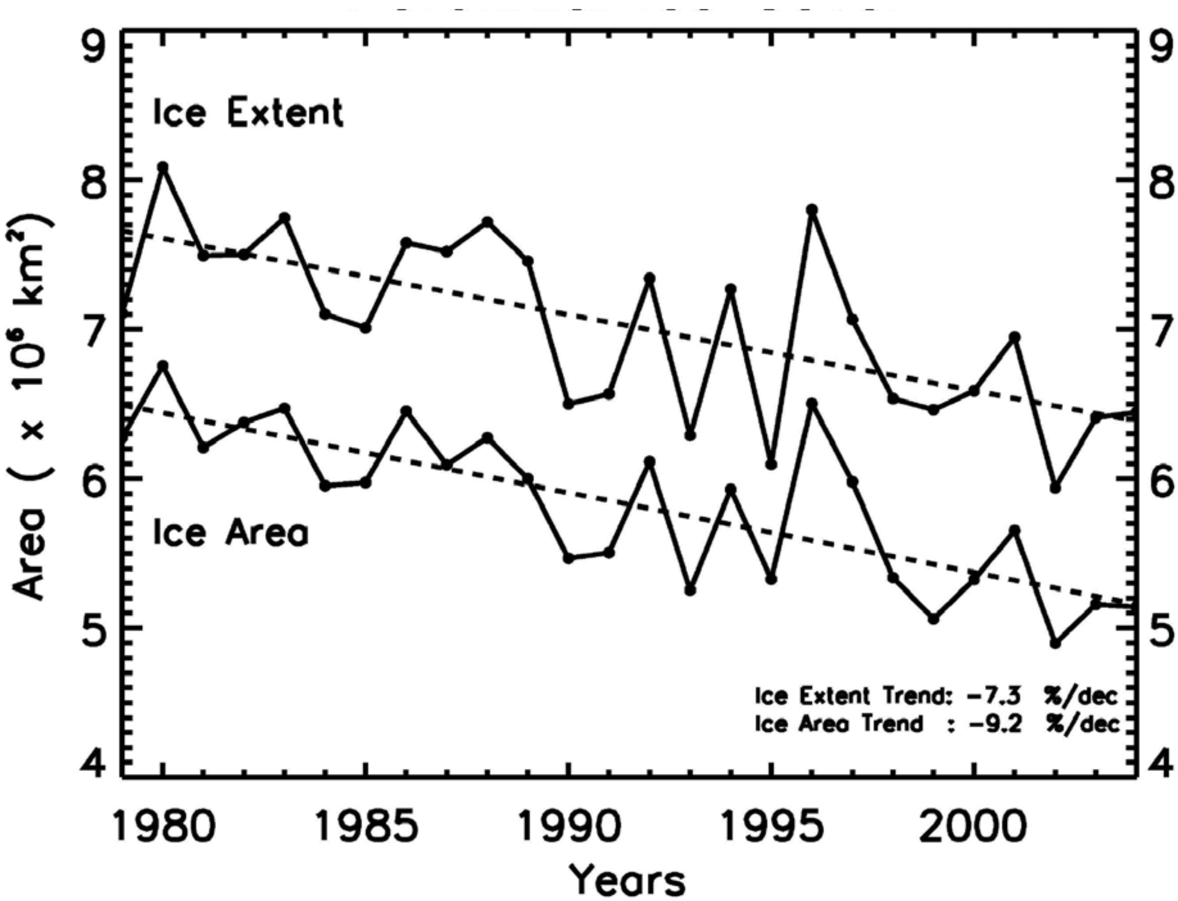

Figure 4.4.2. Yearly extent and area of the summer minimum Arctic ice cover from 1979 to 2004. Dashed lines indicate the linear trend (updated from Comiso, 2002)

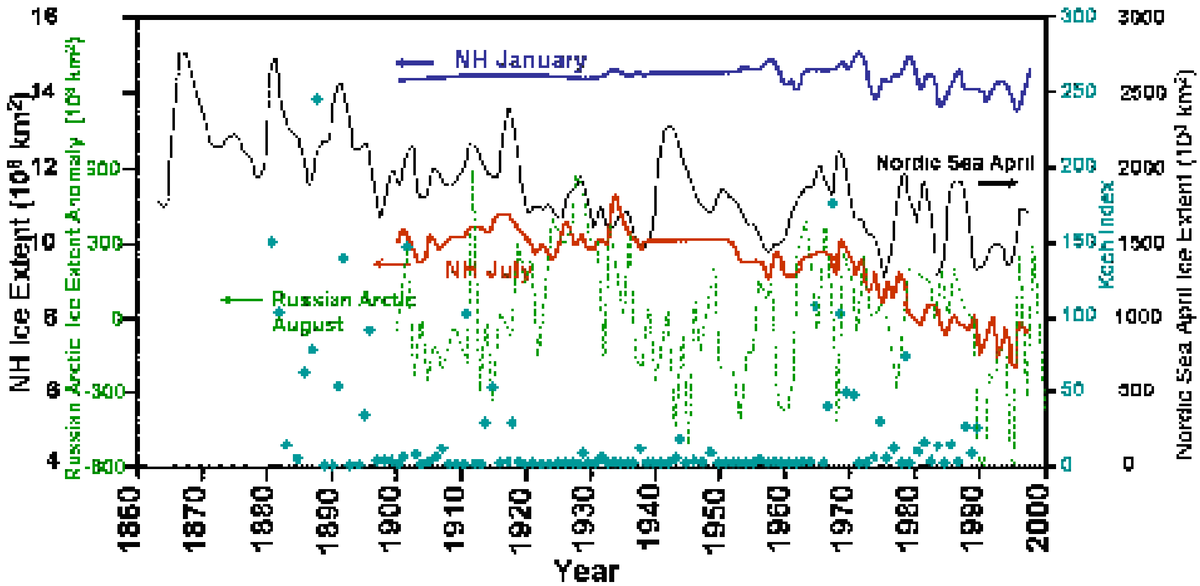

Figure 4.4.3. Time series of Northern Hemisphere ice extent for January and July from the HadISST data set (the blue and red curves, redrafted from Rayner et al., 2003), the April Nordic Sea ice extent (the black curve, redrafted from Vinje, 2001), and the August ice extent anomaly in the Russian Arctic seas -- Kara, Laptev, East Siberian and Chukchi -- the dotted green curve, redrafted from Polyakov et al., (2003). The blue symbols indicate values of the "Koch Index"— an annual function of length of Icelandic coastline experiencing ice each year and the duration of ice persistence (redrafted from Ogilvie and Jónsson, 2001).

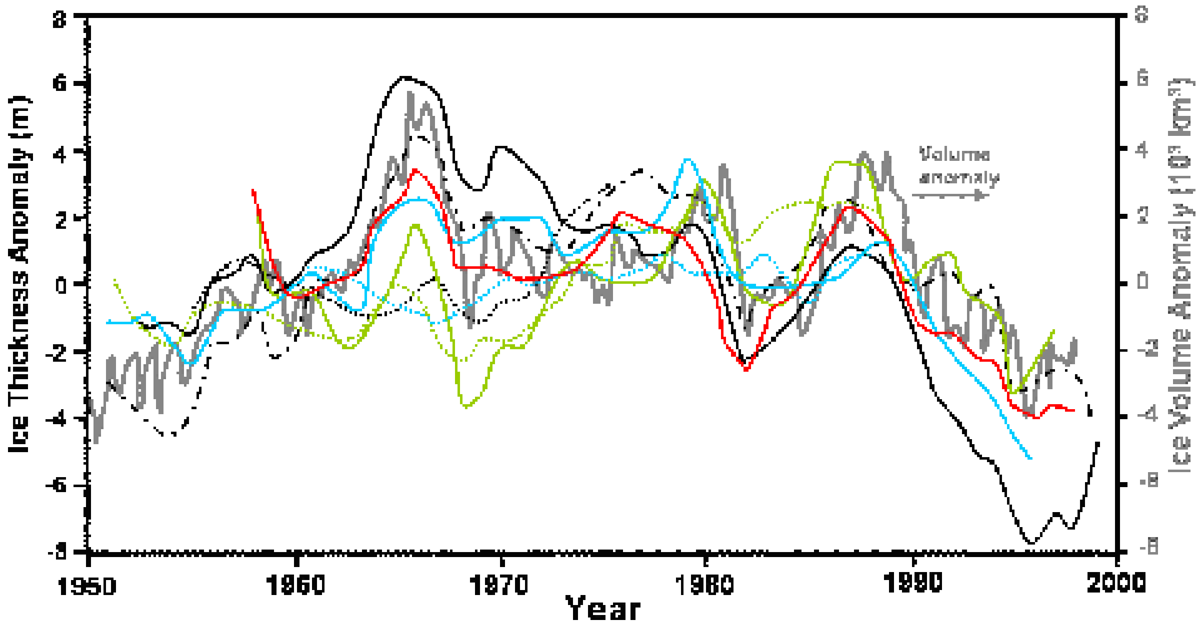

Figure 4.4.4. Comparison of model-based time series of annual mean, Arctic-basin average ice thickness anomaly), obtained from a variety of models (redrafted from Rothrock et al., 2003 – see this paper for identification of the individual models and their attributes), along with the Arctic basin ice volume anomalies (grey curve and right-hand scale) comptuted by Koeberle and Gerdes (2003).

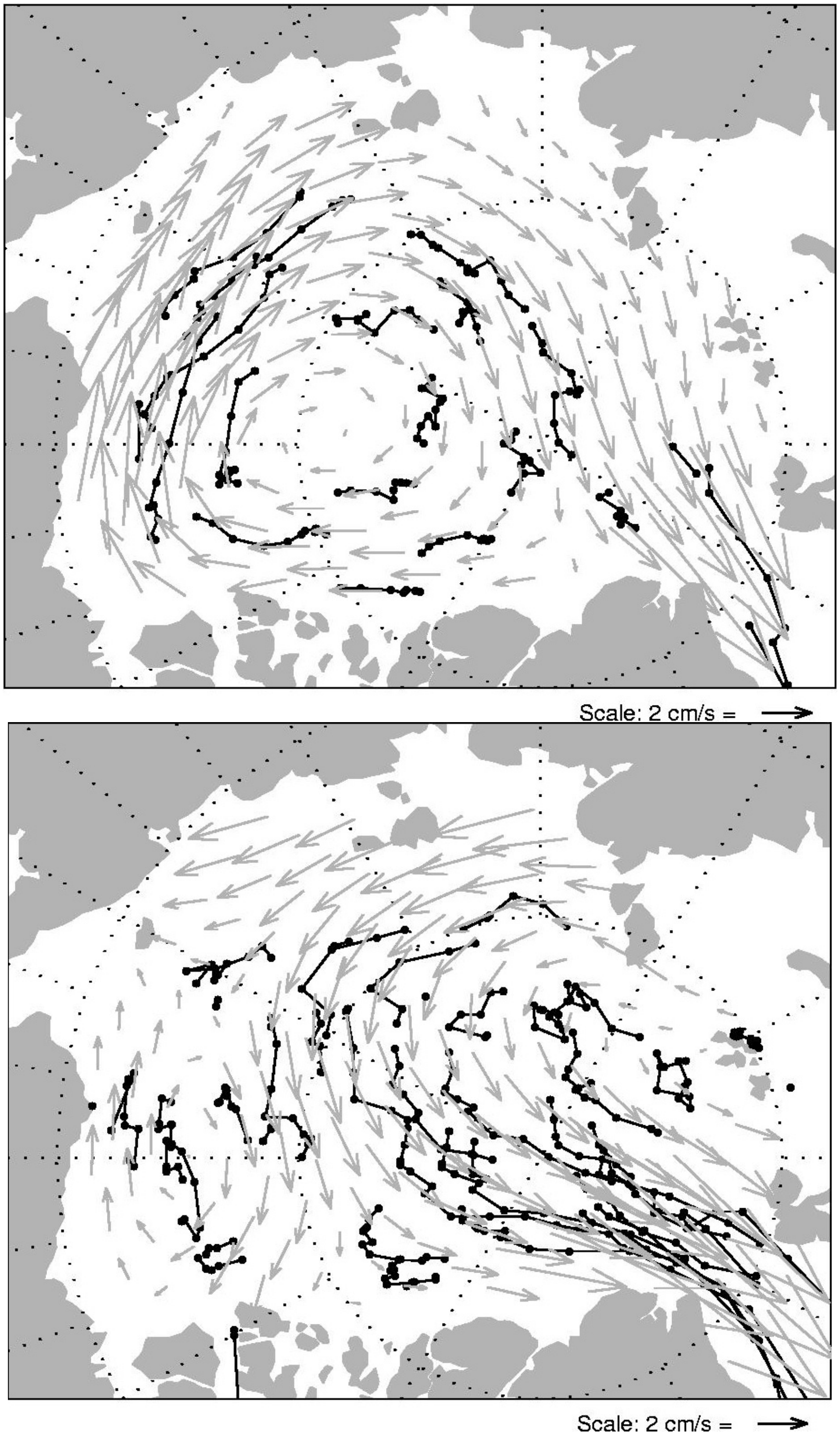

Figure 4.4.5. These maps show the monthly positions of buoys and analyzed field of sea-ice motion for 1979 (top) and 1994 (bottom), from Rigor et al. (2002).

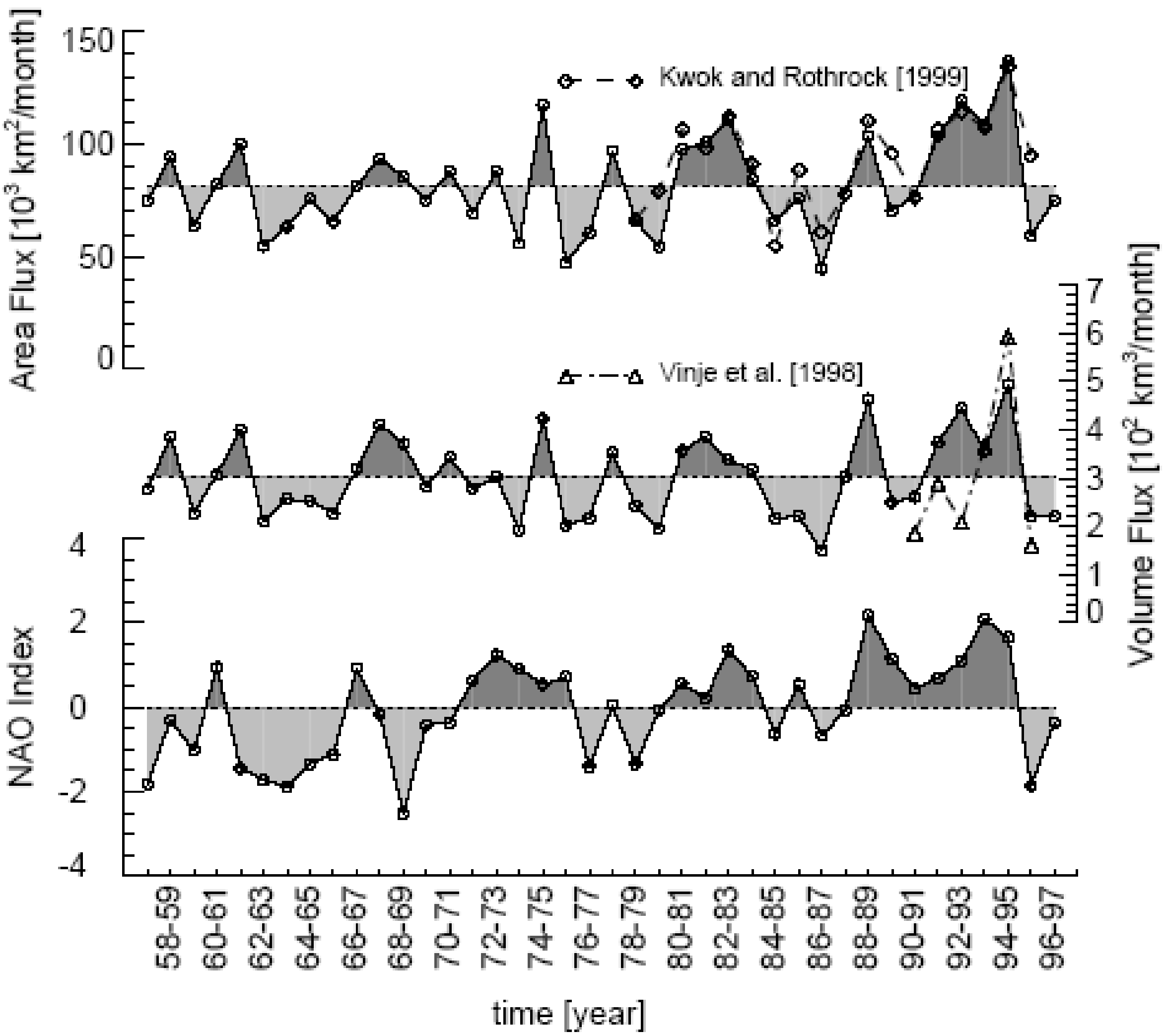

Figure 4.4.6. Time series of modelled Fram Strait area and volume flux, along with NAO index. Also shown are observational estimates of area flux (Kwok and Rothrock, 1999) and volume flux (Vinje et al., 1998). This figure is reproduced from Hilmer and Jung (2000).

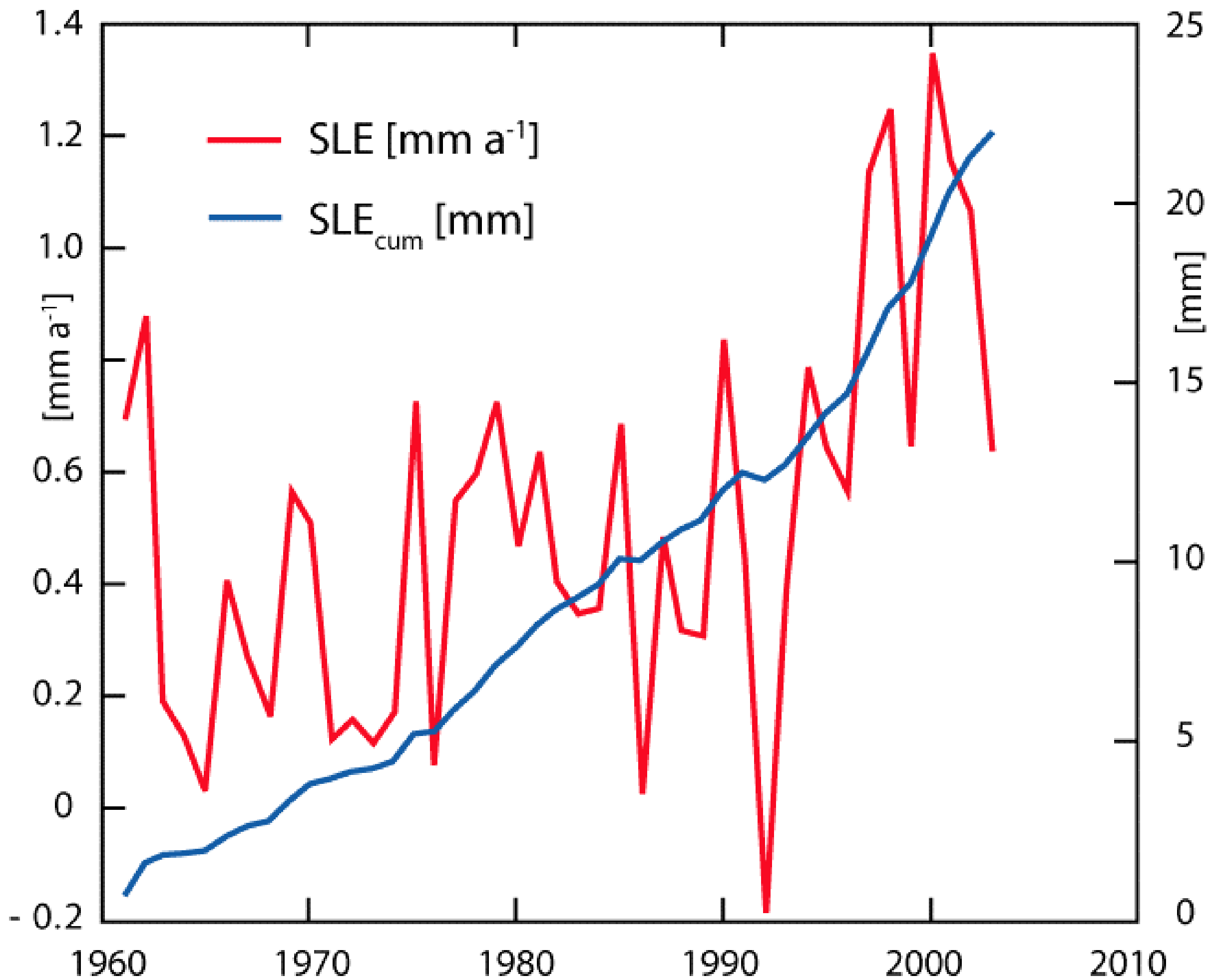

Figure 4.5.1. Annual and cumulative sea level equivalents, SLE, of G&IC changes including those surrounding the ice sheets (Dyurgerov and Meier, 2005).

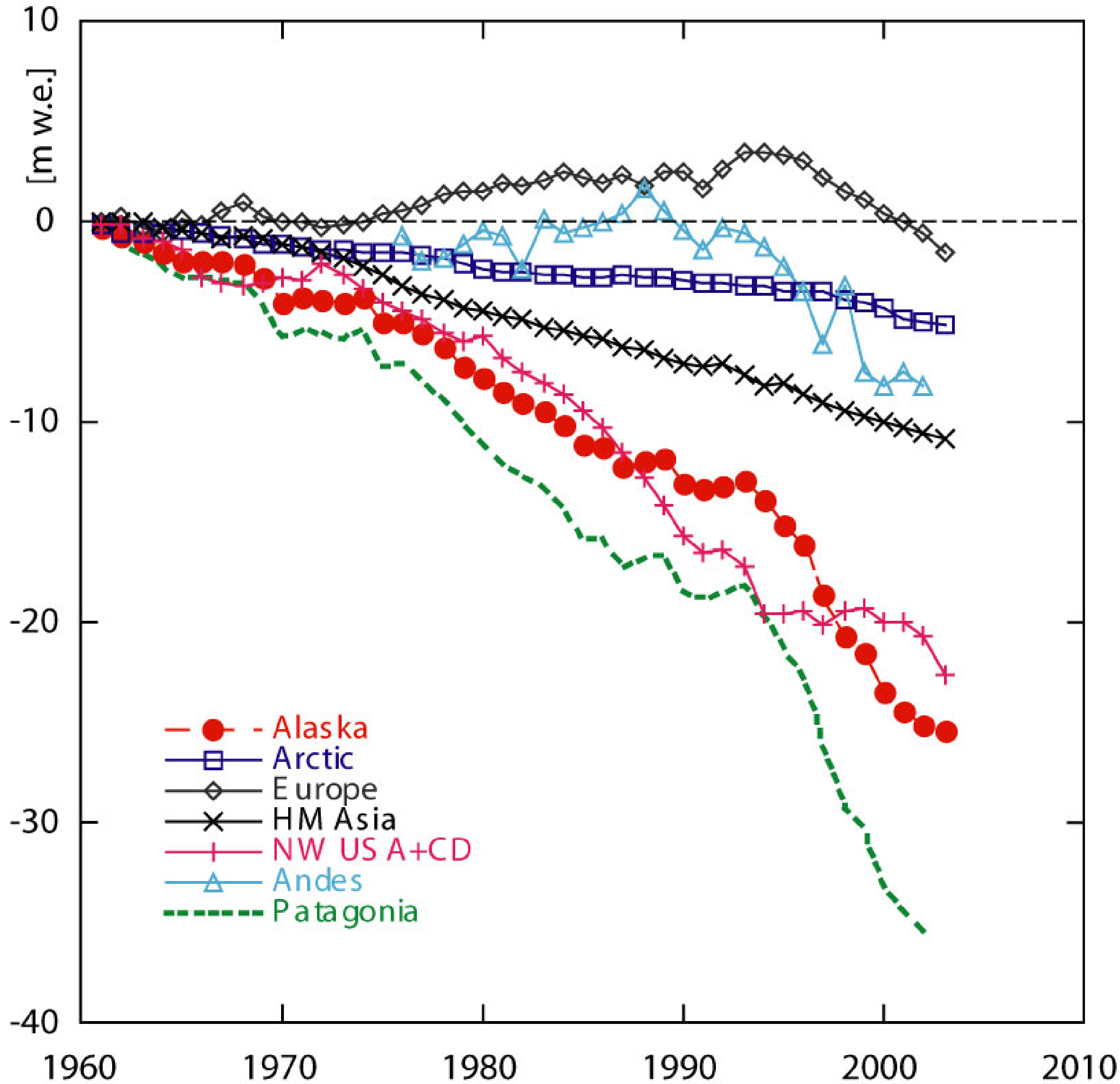

Figure 4.5.2. Cumulative specific mass balance of G&IC in meters water equivalent, calculated for large regions (Dyurgerov and Meier, 2005).

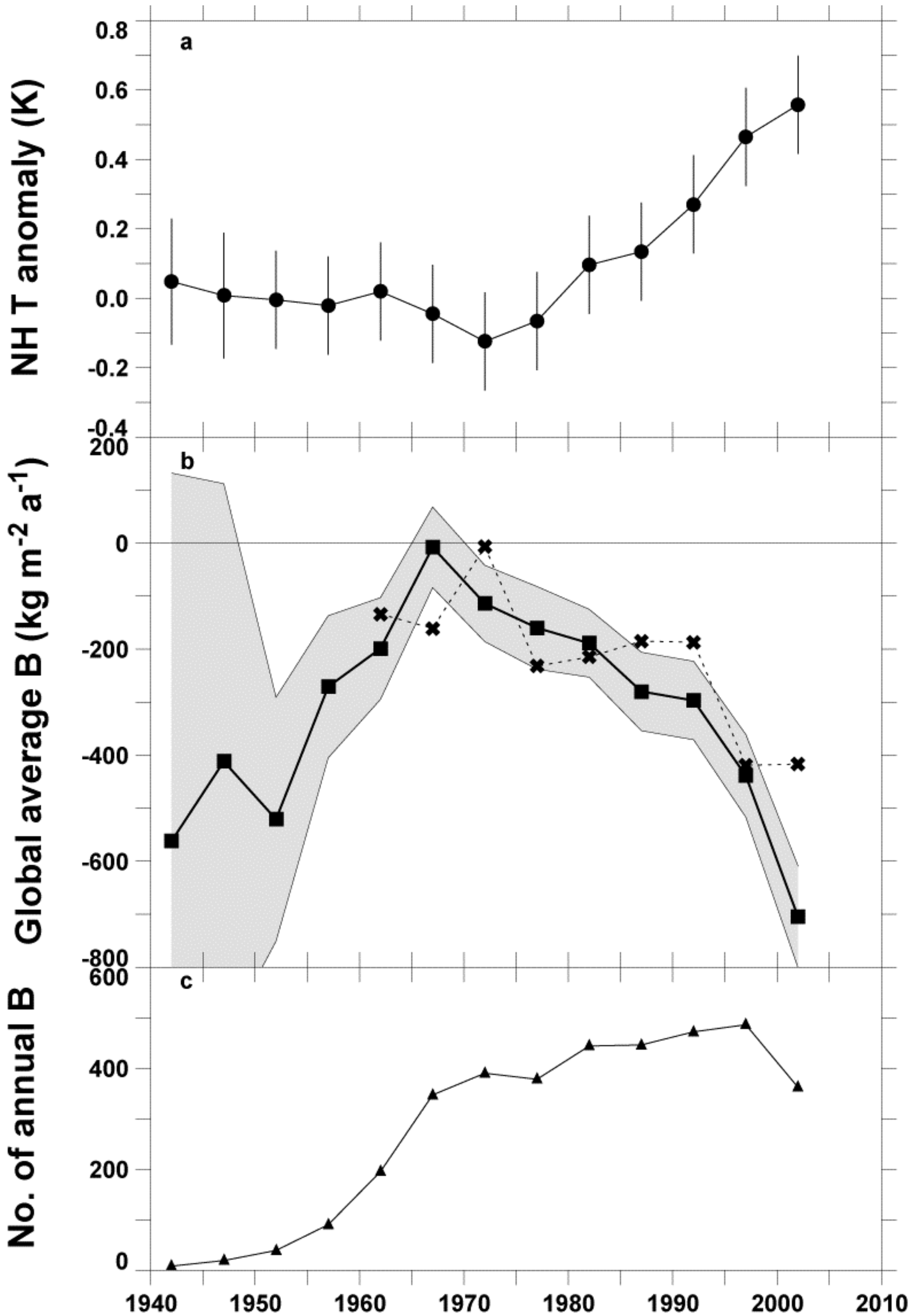

Figure 4.5.3. Pentadal average mass balance of the world's glaciers and ice caps for the last half century, excluding those in Antarctica. Squares: arithmetic averages, weighted by standard errors of single-glacier measurements (grey shading). Crosses: estimates which correct for spatial bias by interpolation at unmeasured locations. Spatially interpolated values correlate well highly with Northern Hemisphere temperatures, arithmetic means only slightly less. Triangles: number of single-glacier balance measurements per pentade (70–90 year recently). For the most recent pentade, 2000–2004, reports are not complete (Cogley, 2005).

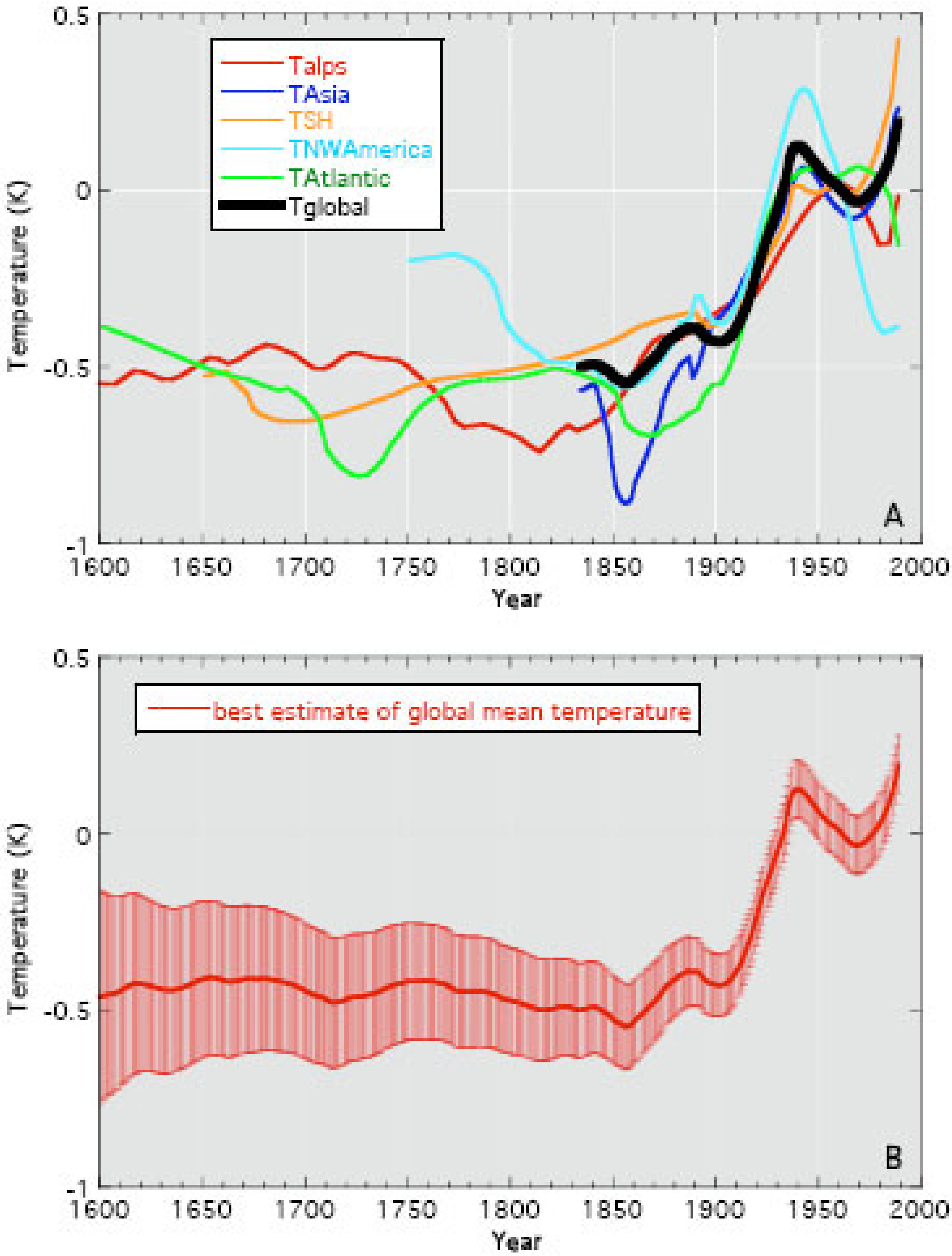

Figure 4.5.4. (A) Temperature reconstruction from glacier length variations for various regions. The black curve shows an estimated global mean value, obtained by giving weights of 0.5 to the Southern Hemisphere, 0.1 to Northwest America, 0.15 to the Atlantic sector, 0.1 to the Alps and 0.15 to Asia. (B) Best estimate of the global mean temperature obtained by combing the weighted global mean temperature after 1834 with the stacked temperature record before 1834. The band indicates the estimated standard deviation (Oerlemans, 2005).

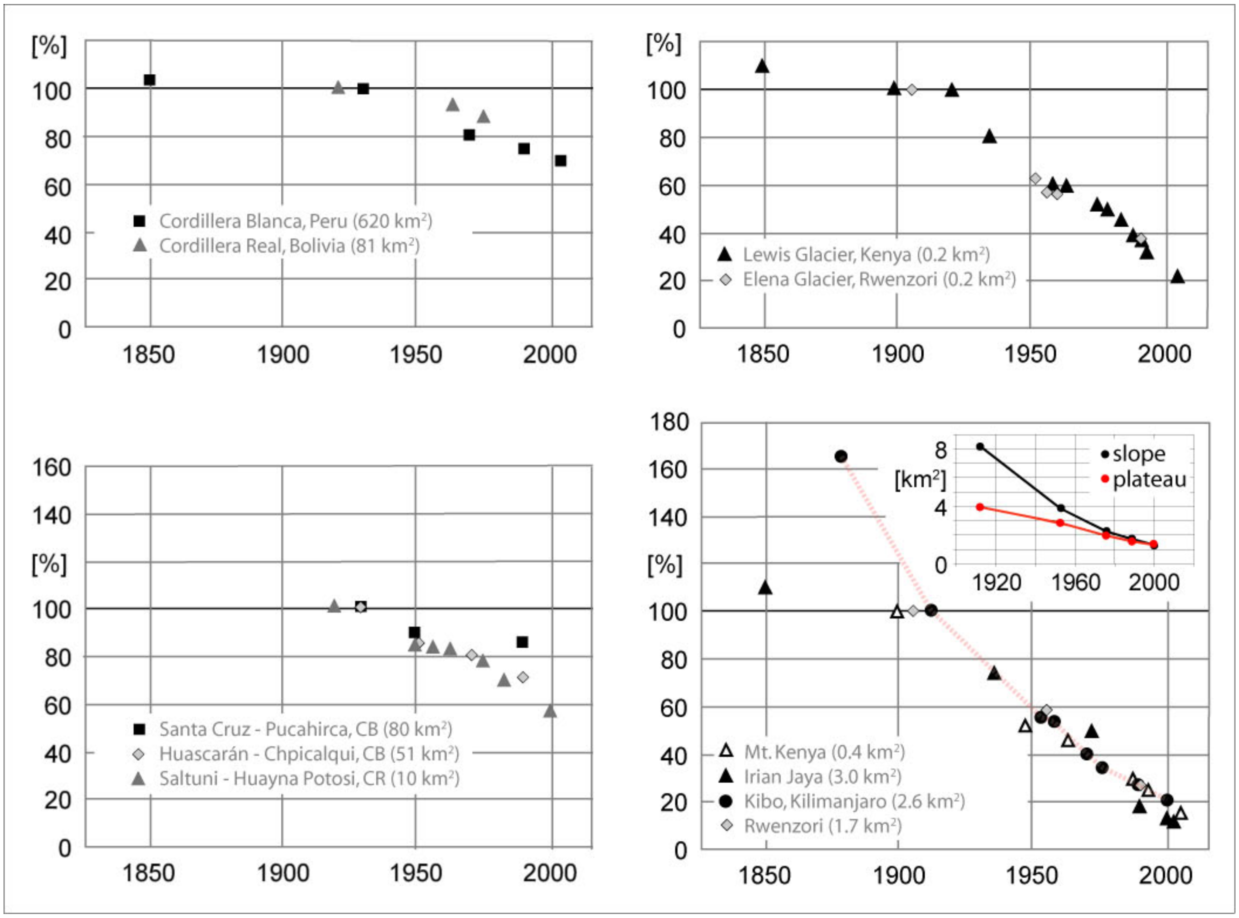

Figure 4.5.5. Changes in surface area of tropical glaciers relative to their extent around 1900, grouped according to different glacier sizes (appr. 1990). The broken red line highlights the retreat of Kilimanjaro glaciers. The small insert shows the absolute area change of Kilimanjaro plateau (red) and slope (black) glaciers as separated by the 5700 m contour line. (Georges, 2004; Hastenrath, 2005; Kaser and Osmaston, 2002; Mölg et al., 2003; Thompson et al., 2002) Additional data are from A. Klein and S. Lieb.

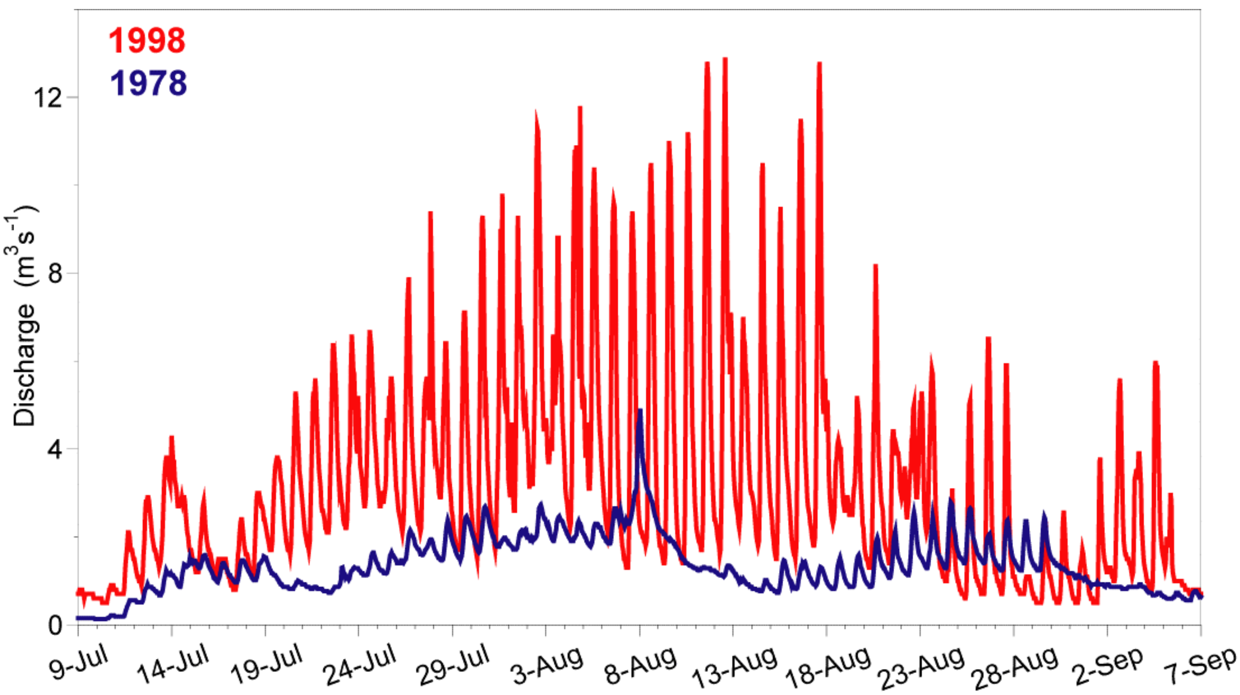

Figure 4.5.6. Observed effects of prolonged glacier mass loss on daily discharge of Vernagtferner, Austria. Moderate summer discharge totals, peak flows and diurnal amplitudes during the 1970s, when positive mass balances prevailed, were significantly enhanced by the end 1990s due to a two-decade period of continuous glacier mass loss in general and a loss of the firn cover in particular. (Data source: Bavarian Academy of Science, Glaciology, http://www.glaziologie.de/).

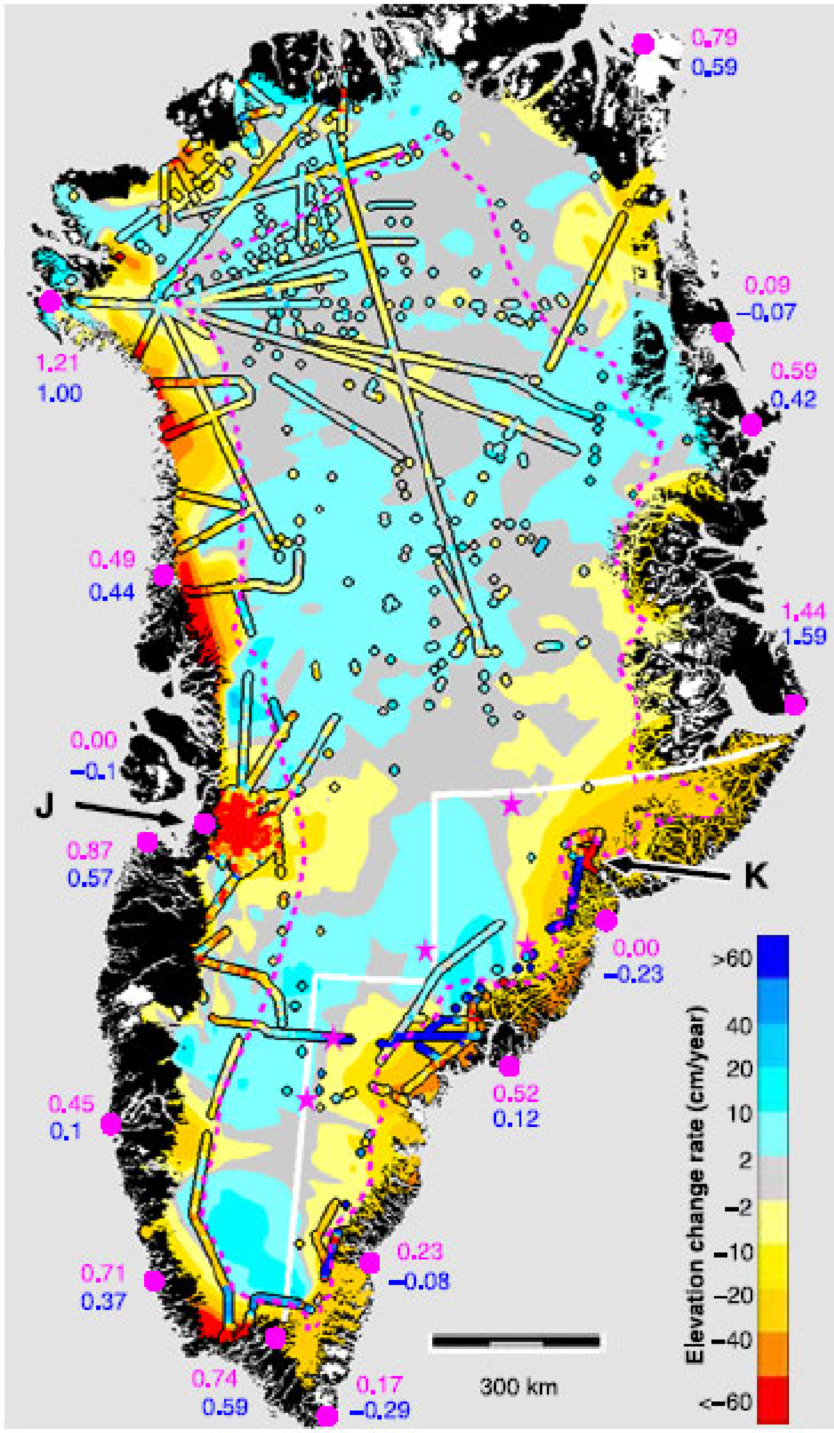

Figure 4.6.1. Rates of elevation change along ATM flight lines during 1997–2003, superimposed on a map of elevation-change rates resulting from the 1993/1994 and 1998/1999 surveys (Krabill et al., 2000). Differences between average summer temperatures (June/July/August), and those for 1961–1990, are listed at coastal weather stations, for 1997–2002 (upper) and 1993–1999 (lower). The region outlined in the southeast consistently thinned until 2001, and then thickened substantially between May 2001 and May 2003. "J" and "K" show Jakobshavn Isbrae and Kangerdlugssuaq Gletscher. The broken line indicates the 2000 meter contour. Ice cores discussed in the text are marked by stars (from Krabill et al., 2004).

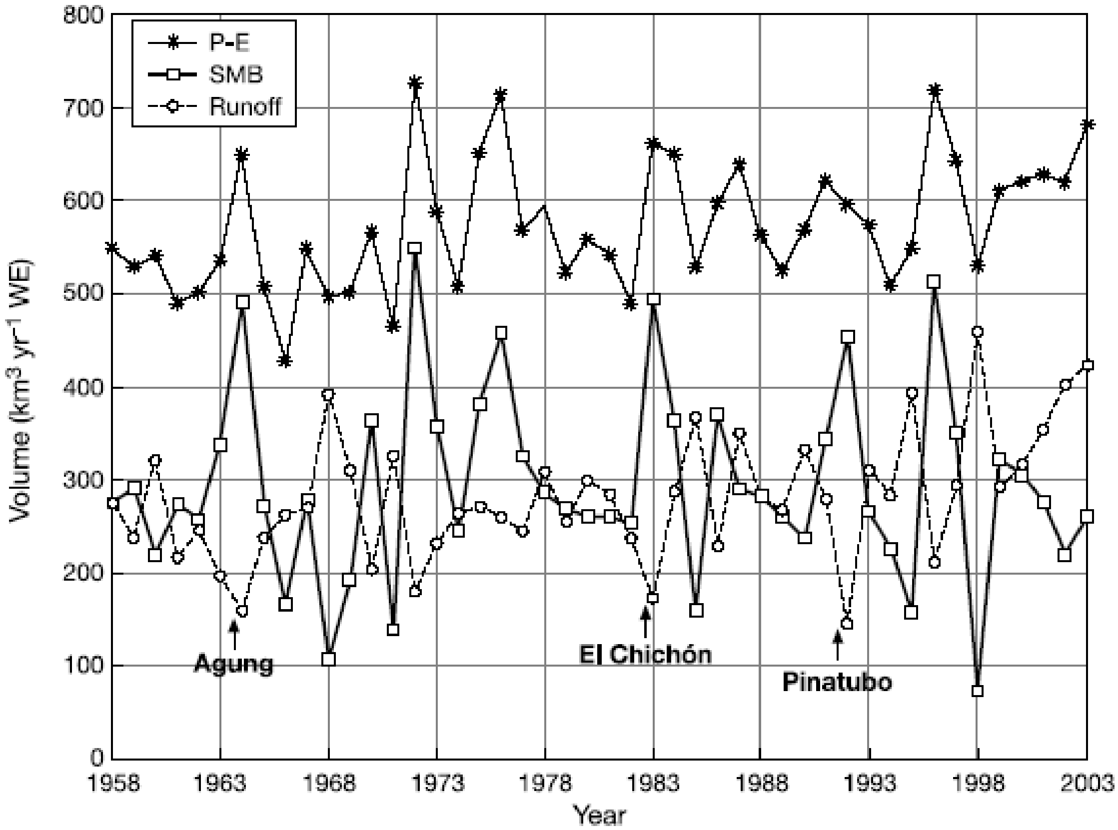

Figure 4.6.2. Greenland ice sheet surface mass balance series for past 46 years (from Hanna et al., 2005).

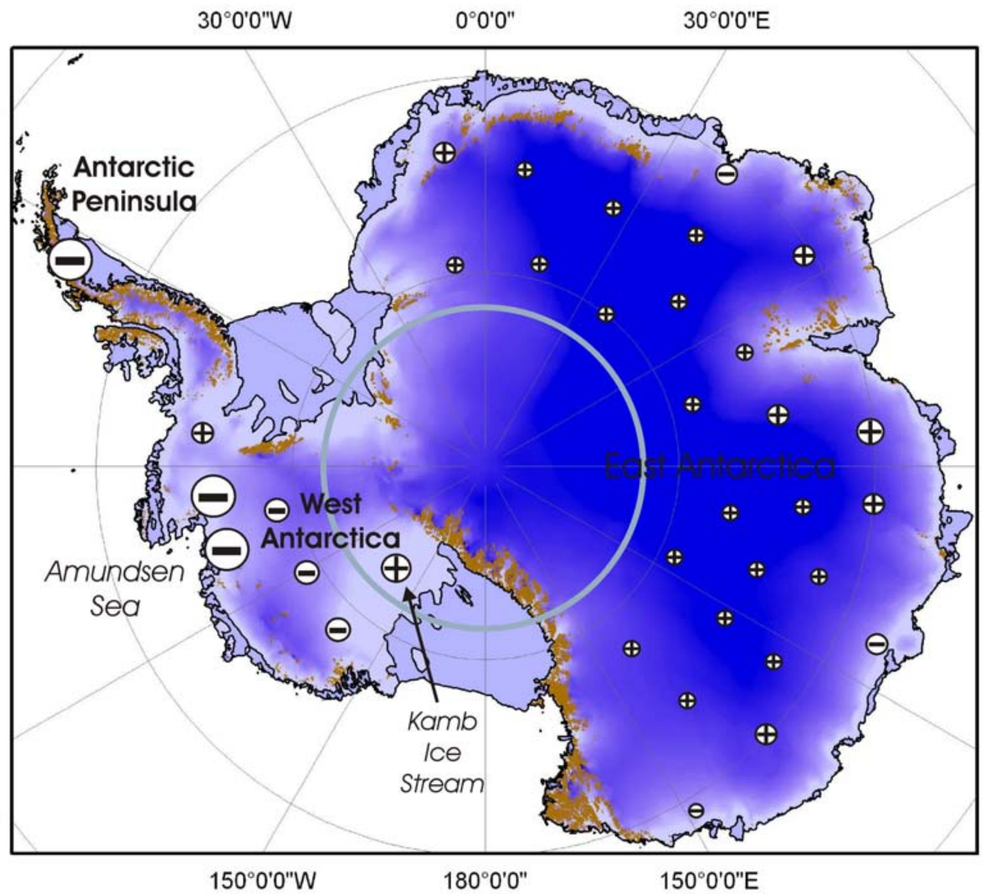

Figure 4.6.3. Modes of mass imbalance of the Antarctic ice sheet (from Vaughan, 2005).

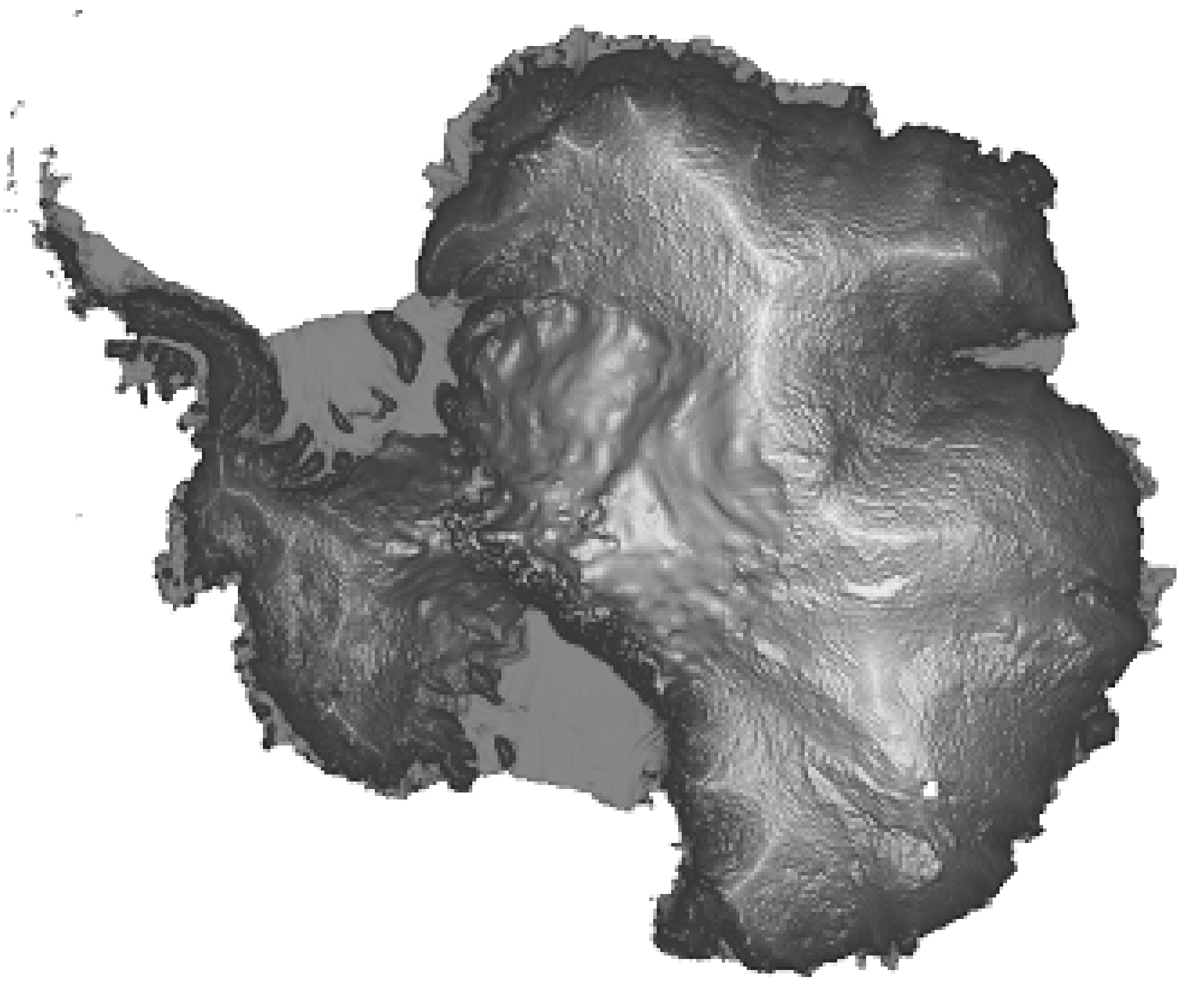

Figure 4.6.4. A digital elevation model of Antarctica. Ice shelves can be clearly identified as regions of a uniform, light grey colour (Bamber and Bindschadler, 1997).

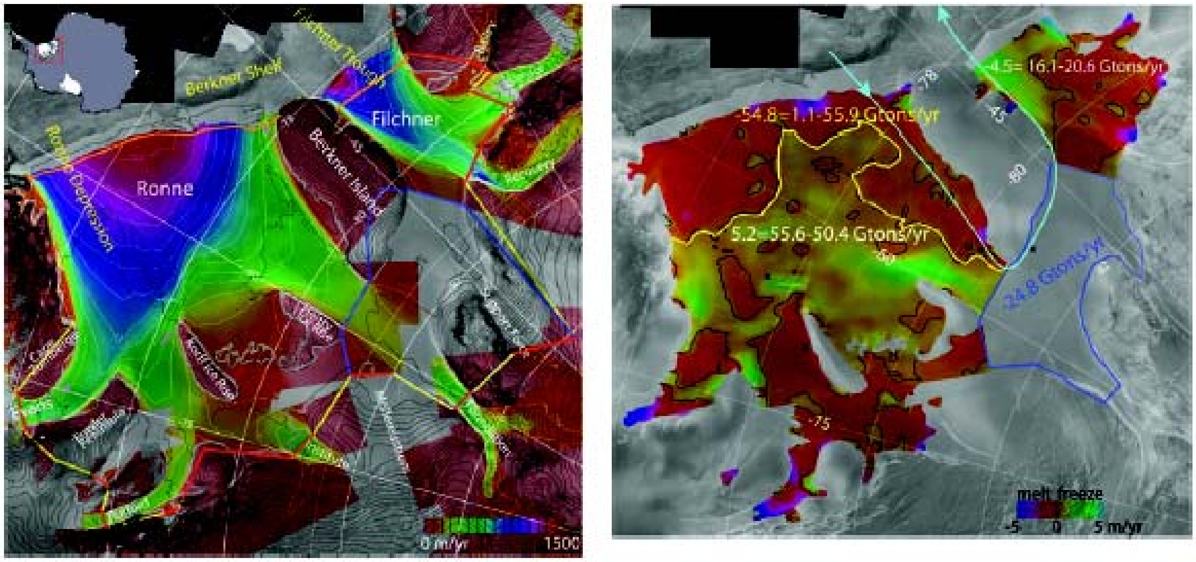

(a) **(b)**

Figure 4.6.5. (From Joughin and Padman, 2003) **(a)** Ice flow speed (colour and 100 m yr^{-1} white contours) for the Filchner Ronne Ice Shelf determined using Interferometric Synthetic Aperture Radar and speckle-tracking with tidal corrections on the floating ice. Surface elevation 100-m contours (black) are plotted over the SAR base map image (Jezek, 1999). The velocity data show the September 2000 ice front, while the base map shows the September 1997 front. **(b)** Basal melt rates (colour) determined under assumptions of conservation of mass and of a steady-state ice shelf (Jenkins and Doake, 1991). The colour bar saturates at magnitudes >5 m yr^{-1}. Negative values imply melt and positive values freezing. Light blue lines show inferred ocean circulation paths (Nicholls et al., 2001).

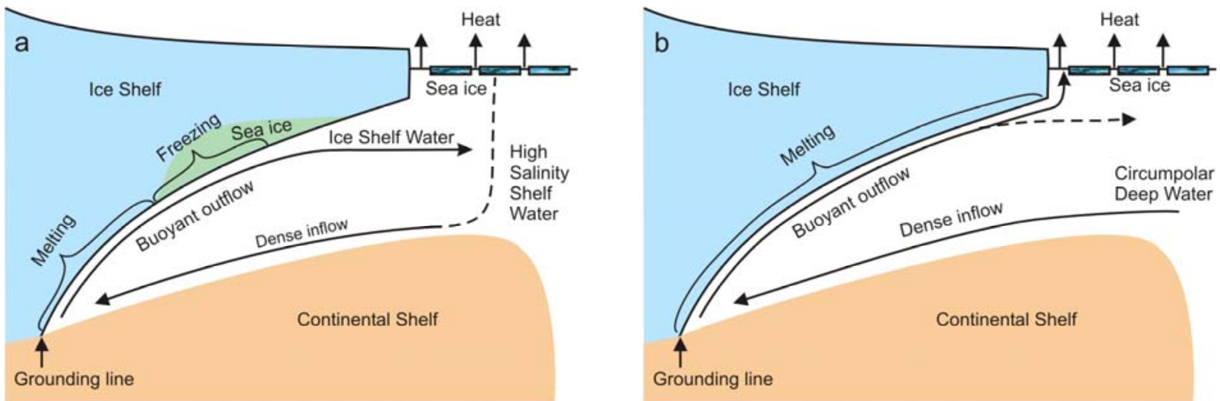

Figure 4.6.6. Two modes of sub-ice-shelf circulation: a) on a continental shelf dominated by High Salinity Shelf Water (HSSW); b) on a continental shelf dominated by Circumpolar Deep Water (CDW).

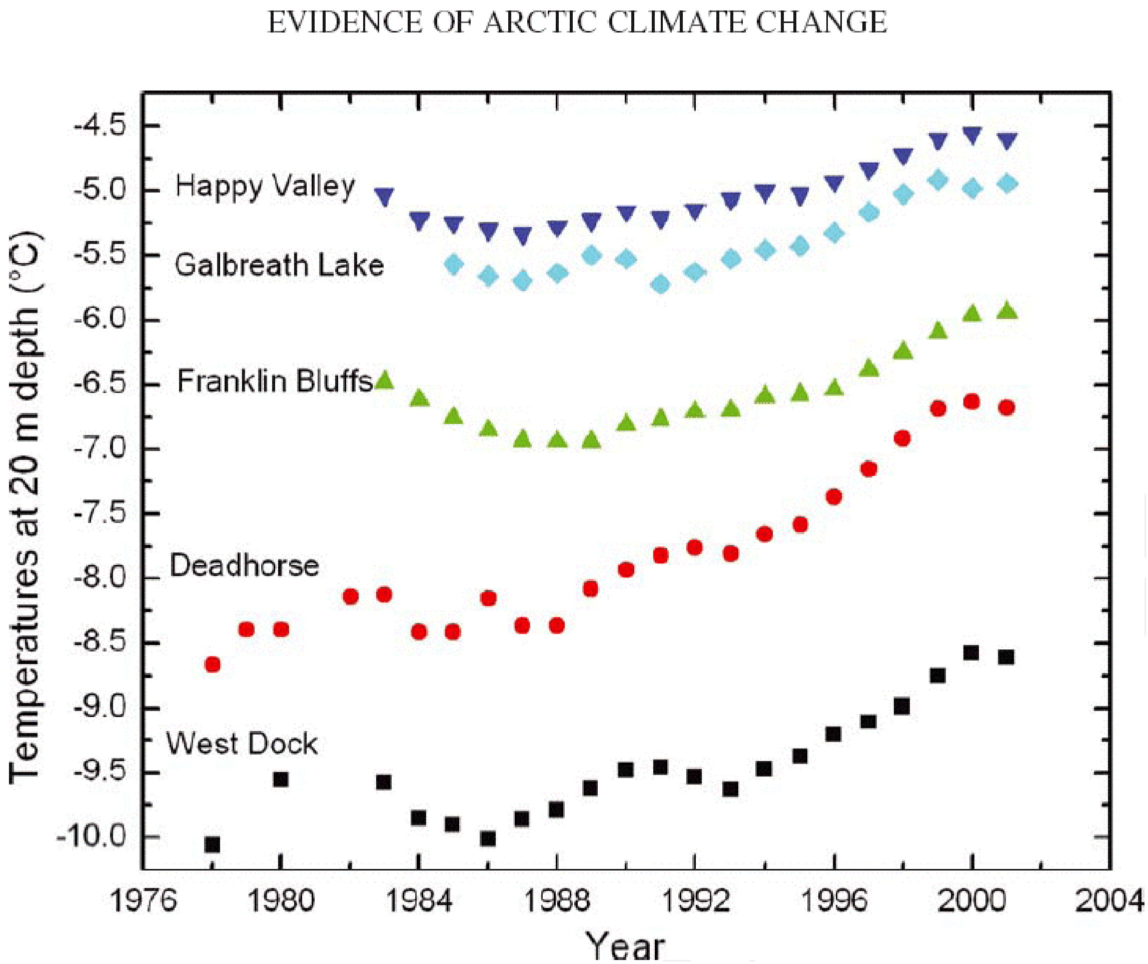

Figure 4.7.1. Temperature measured at the 20 m depth in boreholes in permafrost on the North Slope of Alaska display broad scale warming over recent decades (Osterkamp, 2003).

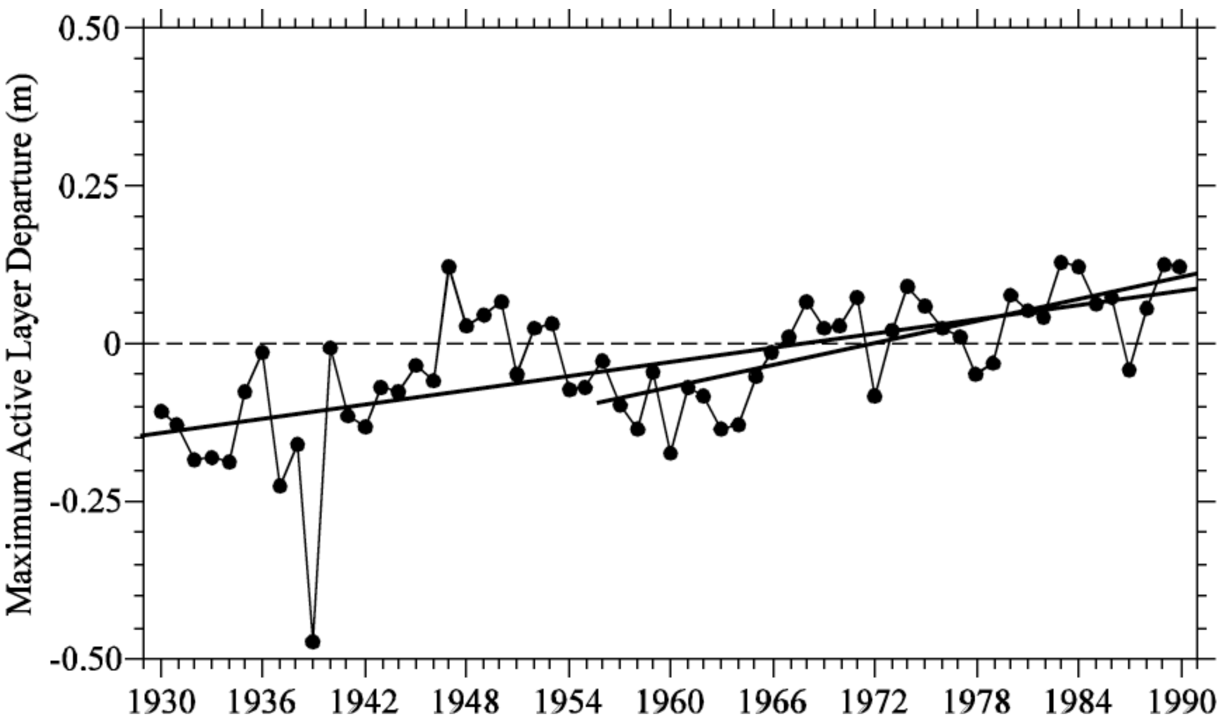

Figure 4.7.2. Changes in active layer thickness in the Russian Arctic (Frauenfield et al., 2004).

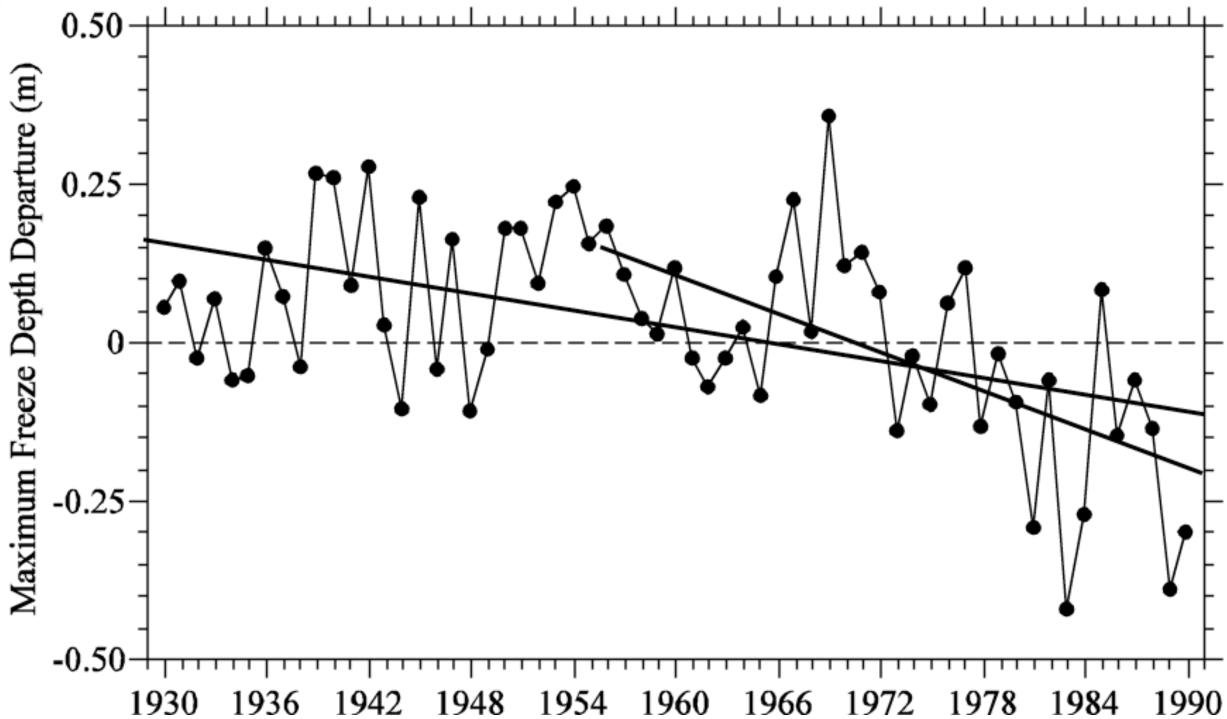

Figure 4.7.3. Changes in seasonally frozen ground depth in the former Soviet Union (Frauenfeld et al., 2004).

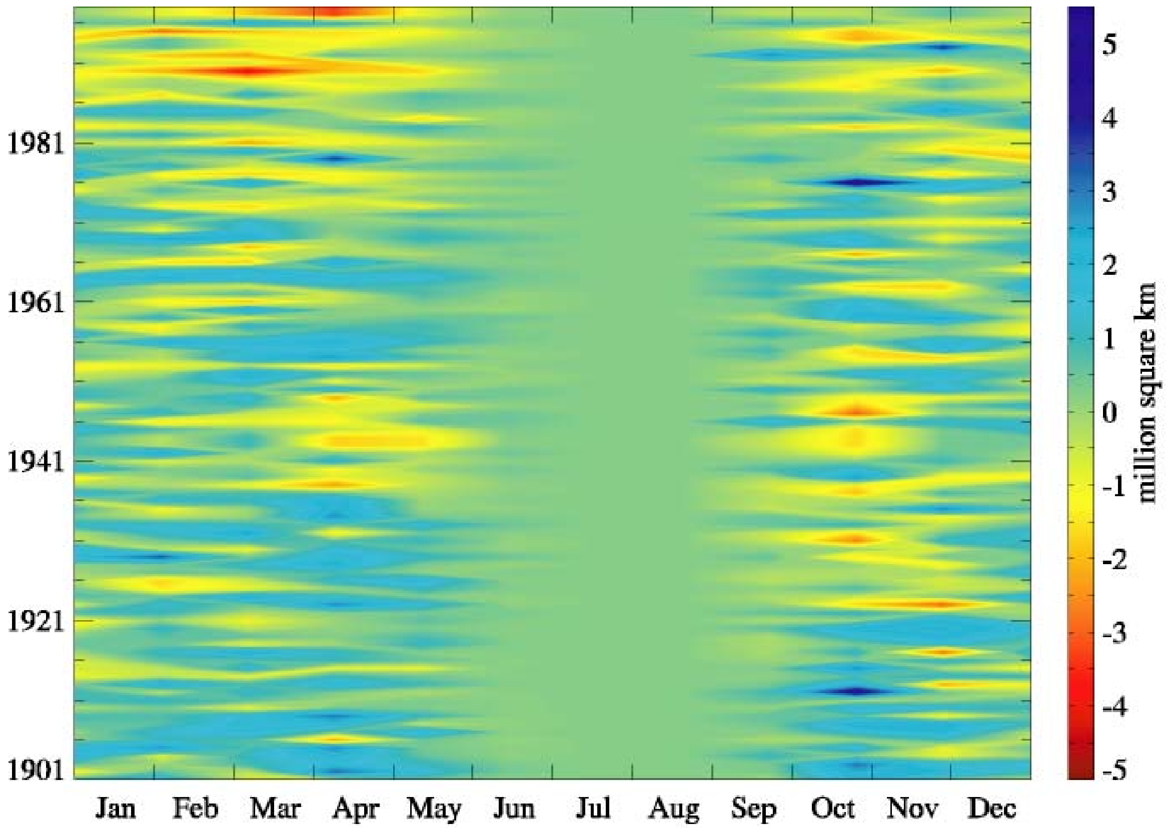

Figure 4.7.4. Changes in areal extent of seasonally frozen ground in the Northern Hemisphere (Zhang et al., 2005).

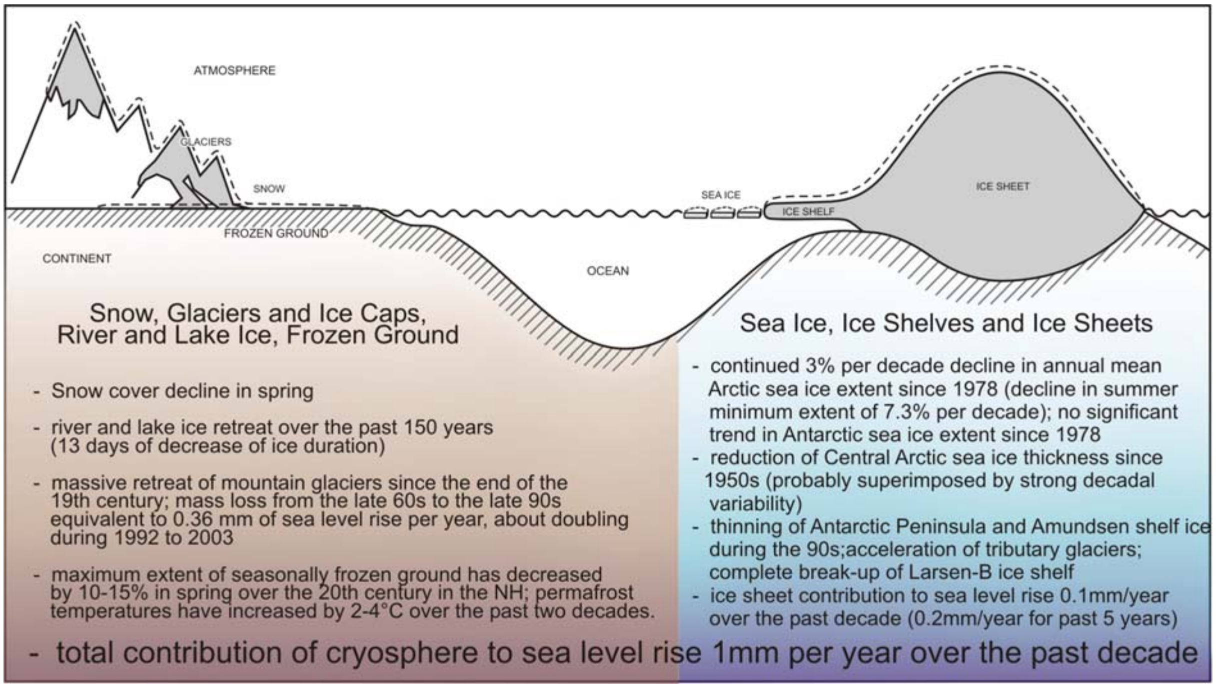

Figure 4.8.1. Summary of observed variations of the cryosphere.

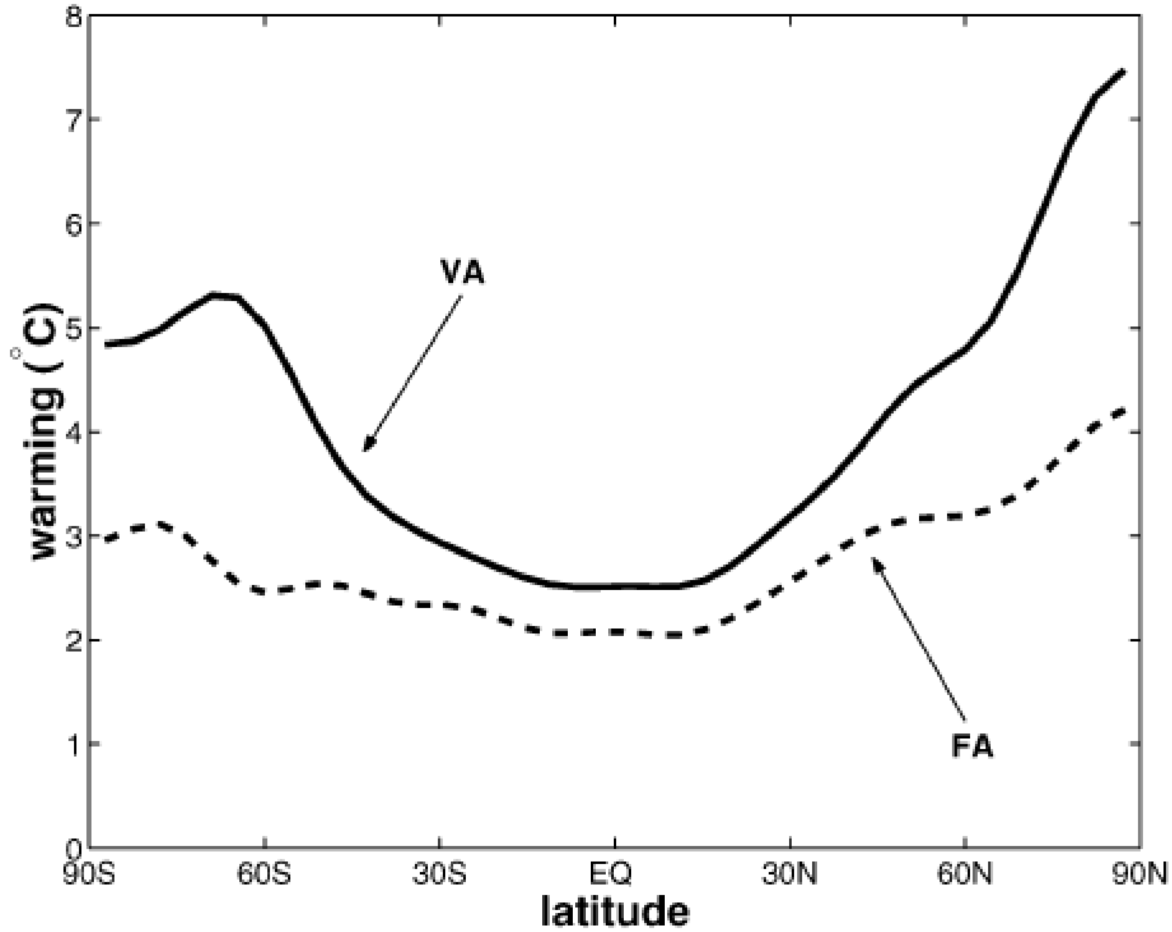

Box 4.1, Figure 1. The quasi-equilibrium zonal-mean, annual-mean warming resulting from CO_2 doubling in the experiment with fixed albedo (FA, dashed line) and with surface albedo feedback included (VA, solid line) models (from Hall, 2004).

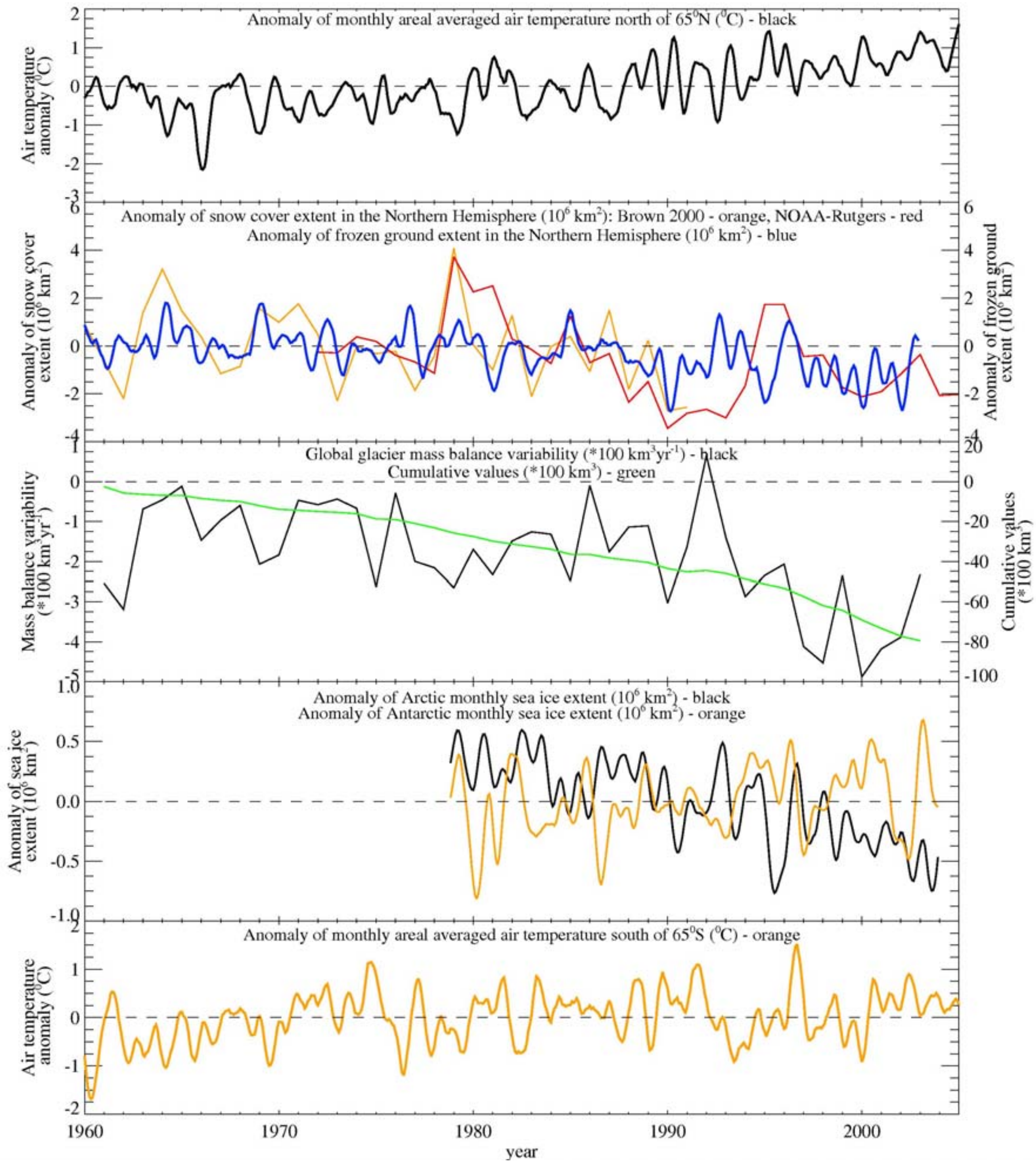

Question 4.1, Figure 1. Time series of surface air temperature (updated from Jones and Moberg, 2003), glacier mass balance (Dyurgerov and Meier, 2005), and the extent of snow cover (Brown, 2000; updated from Armstrong and Brodzik, 2001), frozen ground (Zhang et al., 2005) and sea ice (updated from Comiso, 2003).